galaxies

MDPI

Article

Dark Matter Dogma: A Study of 214 Galaxies

Alan Sipols [1] and Alex Pavlovich [2,*]

[1] Independent Researcher, London NW8, UK; alansipols@gmail.com
[2] Independent Researcher, Glenview, IL 60025, USA
* Correspondence: axlpav@gmail.com

Received: 25 February 2020; Accepted: 21 April 2020; Published: 28 April 2020

Abstract: The aim of this paper is to test the need for non-baryonic dark matter in the context of galactic rotation and the apparent difference between distributions of galactic mass and luminosity. We present a set of rotation curves and 3.6 μm surface brightness profiles for a diverse sample of 214 galaxies. Using rotation curves as the sole input into our Newtonian disk model, we compute non-parametric radial profiles of surface mass density. All profiles exhibit lower density than parametric models with dark halos and provide a superior fit with observed rotation curves. Assuming all dynamical mass is in main-sequence stars, we estimate radial distributions of characteristic star mass implied by the corresponding pairs of density and brightness profiles. We find that for 132 galaxies or 62% of the sample, the relation between density and brightness can be fully explained by a radially declining stellar mass gradient. Such idealized stellar population fitting can also largely address density and brightness distributions of the remaining 82 galaxies, but their periphery shows, on average, 14 $M_{\odot}/pc^2$ difference between total density and light-constrained stellar density. We discuss how this density gap can be interpreted, by considering a low-luminosity baryonic matter, observational uncertainties, and visibility cutoffs for red dwarf populations. Lastly, we report tight correlation between radial density and brightness trends, and the discovered flattening of surface brightness profiles—both being evidence against dark matter. Our findings make non-baryonic dark matter unnecessary in the context of galactic rotation.

Keywords: galaxy; rotation curve; Newtonian dynamics; galaxy mass model; surface mass density; surface brightness; mass–luminosity; radial star mass profile; dark matter

1. Introduction

Elevated to the status of an axiomatic assumption, the concept of dark matter has settled firmly in modern astrophysics and cosmology. Galactic mass templates presuppose dark halos, with debates mostly focusing on their features such as "core-cusp problem" [1–3] rather than questioning their existence. Dark matter rush burgeons with state-of-the-art experiments [4–7] and theories on the nature of the alleged enigmatic substance [8–10]; but is there an impeccable basis for the excitement? Has empirical evidence of anomalous phenomena been established beyond a reasonable doubt, backed by a wealth of strong data and realistic assumptions? If so, then have alternative simpler explanations been exhausted? What if dark matter is regular baryons obscured by observational limitations and analytical habits? Considerations like these inspired us to write this paper.

Our focus here is on the apparent difference between expected mass distribution and luminosity in galaxies, which is one of the main reasons for the dark matter hypothesis. It has been widely reported that in most galaxies, light intensity declines faster than mass density[1] away from the center [11–14]. Consequently, the implied mass-to-light (M/L) ratio is orders of magnitude higher at the periphery than at the center. There were many attempts to explain M/L gradient with various forms

[1] Unless explicitly specified otherwise, we use the term "*density*" to refer to "*surface mass density*", for brevity.

of non-luminous baryonic matter including brown dwarfs [15], black holes [16,17], and fractal cold hydrogen [18,19], to name a few. Yet, these ideas never fully addressed the problem, and dark matter in a form of unknown, non-baryonic substance became a commonly accepted explanation[2]. Most of its proponents theorize that dark matter accounts for several times [25–28] more mass than baryonic matter. Despite intensive search however, all attempts to detect non-baryonic dark matter so far failed.

In a 2014 paper [29], we presented a Newtonian thin disk model for deriving radial distributions of mass directly from galactic rotation curves (RC). Applied to a set of 47 galaxies, the model produced mass estimates lower than those in the literature. We have subsequently refined the model, expanded the galaxy sample to 214, and used 3.6 μm luminosity data as an independent constraint to identify differences between total density and light-constrained stellar density. We present our methods, data, and results in the corresponding sections of this paper. Our conclusion is that the need for dark matter was artificially inflated by the dominant analytical approach, and that dark matter is unnecessary to model galactic rotation and to explain the sliding M/L phenomenon.

2. Methods

2.1. General Approach

Our approach to M/L problem is straightforward—we compute radial distributions of surface mass density and compare them to respective surface brightness profiles. There are two aspects of our method, different from the traditional approach, that ensure a fair basis for exploring the M/L problem. First, rather than using popular parametric modular templates to infer density from brightness, we compute non-parametric dynamical density profiles directly and solely from RCs, using a thin disk model. Second, we avoid making apriori assumptions about a stellar M/L profile and speculative dark halo. Instead, we match two independent datasets—the computed density and the observed brightness profiles, deriving implied radial gradients of characteristic star mass that fit both density and light data, serving as a test for dark matter in galaxies. Below we explain the mechanics and discuss the merits of this approach.

2.2. Incumbent Component Models

Conventionally, mass distribution is modeled analytically, treating a galaxy as a set of conspiring standard components inferred from the shape of surface brightness profile. This is an ambiguous procedure [30], which suffers, in addition to reliance on surface brightness data, from two major deficiencies—the assumptions of uniform or rigid stellar M/L and presupposition of spherical dark halos. A combination of these unproven assumptions leads to a wide gap between underestimated baryonic matter and overestimated total mass, lending support for dark matter hypothesis.

2.3. Disk Mass Density Model

Considering the deficiencies of incumbent models, what would be a better method for computing galactic mass distribution? We adopt two key principles: (a) a thin disk is a better geometrical approximation for the overall galactic shape than a sphere; (b) galactic mass distribution must be computed solely from rotation data, using Newtonian gravitation and invariant mathematical solution.

We start with the basic idea shown in Figure 1a, where point *A* is any location at the zeroth azimuth of an ultrathin disk and point *B* is any other location in the disk.

[2] Aside from Modified Newtonian Dynamics (MOND) [20,21] and similar theories, we are aware of only a handful of voices challenging the dark matter paradigm [22–24].

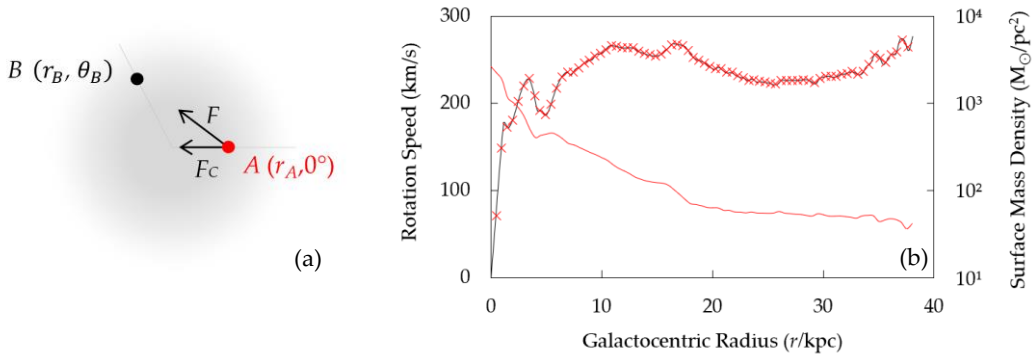

Figure 1. (a) Illustration of the centripetal component of the gravitational force vector. The gravitational force $\vec{F}$ acting on mass at point *A* due to mass at point *B* is shown as the *longer arrow*. Its centripetal component $\overrightarrow{F_C}$ is shown as the *shorter arrow*. **(b)** Illustration of Disk Mass Density Model (DM2) tracking the input rotation curve. The *black solid curve* is M31 galaxy rotation curve from Chemin et al. 2009 [31]. *The red solid curve* represents the surface mass density profile generated by DM2 based on the input rotation curve. *Red crosses* represent the reverse conversion of the computed density profile back into a rotation curve.

The gravitational force $\vec{F}$ acting on mass at point *A* due to mass at point *B* has a centripetal (or centrifugal) component $\overrightarrow{F_C}$ with magnitude $F \cos \varphi$, where φ is the angle between vectors $\vec{F}$ and $\overrightarrow{F_C}$. The total centripetal force acting on mass at point *A* is the sum of all centripetal and centrifugal gravitational pulls *due to mass at all other points* in the disk. Assuming uniform circular motion of material at point *A*, and integrating gravitation over all other points in the disk using polar coordinates (r, θ), we can write:

$$\frac{m_A V_A^2}{r_A} = G\, m_A \iint \Sigma_B(r_B,\theta_B) \frac{r_A - r_B \cos\theta_B}{(r_A^2 - 2r_A r_B \cos\theta_B + r_B^2)^{3/2}}\, r_B\, d\theta_B\, dr_B \quad (1)$$

where m_A and V_A are the mass and the orbital speed at point A $(r_A, 0°)$, G is the Newtonian universal constant of gravitation; Σ_B is the surface mass density at point B (r_B, θ_B); $(r_A - r_B \cos\theta_B)/(r_A^2 - 2r_A r_B \cos\theta_B + r_B^2)^{1/2} = \cos\varphi$; $A \neq B$. The differential in polar coordinates includes factor r_B.

In an *axisymmetric* disk, Σ_B is independent of angle θ and varies only radially; we will denote the corresponding radius-specific mass as m_r. Canceling out m_A from both sides of Equation (1), moving Σ_B outside the inner integral, and approximating integrals numerically, we get:

$$\frac{V_A^2}{r_A} = G \sum_r \left(m_r \sum_\theta \frac{r_A - r\cos\theta}{(r_A^2 - 2r_A r\cos\theta + r^2)^{3/2}} \right) \quad (2)$$

Given a rotation curve $V_A(r_A)$ comprised of N datapoints, Equation (2) can be specified for each of the corresponding N orbits. Assuming that galactic mass is distributed across the same N orbits, we get an $N \times N$ linear system with m_r as the only variable ($N \times 1$ column vector, in matrix form). The linear system has a straightforward and unique solution for m_r (see Appendix A for details).

Using this approach, we developed Disk Mass Density Model *(DM2)* for which details are provided in Appendix A. DM2 takes an observed galactic rotation curve as the sole input and converts it, using the above logic, into a surface mass density profile.

Considering that the output density profile is a non-parametric (the sought distribution of mass is not constrained by any predefined function) and invariant algebraic solution, DM2 ensures exact fits to input RCs (see Figure 1b).

Given a disk rather than a spherical setup, DM2 density estimates are approximately 20–40% lower than those derived from models with dark halos. Figure 2 presents the difference in terms of surface mass density and enclosed mass (<*r*).

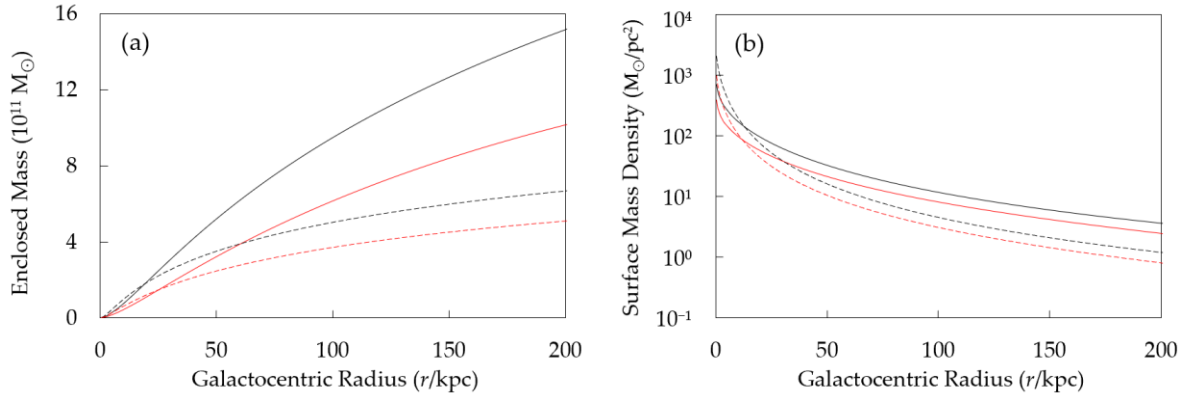

Figure 2. (**a**) *Black dashed curve* replicates Geehan 2006 [32] "best-fitting model" dark halo mass for M31 galaxy, enclosed in a cylinder[3] of radius *r*; *red dashed curve* is the corresponding DM2 disk mass fitting Geehan halo RC. The *Black solid curve* is Sofue 2015 [34] dark halo model mass enclosed in a cylinder (<*r*); the *red solid curve* is the corresponding mass of DM2 disk. (**b**) The *Black dashed curve* is Geehan 2006 halo surface mass density; the *red dashed curve* is the corresponding DM2 disk density. The *Black solid curve* is Sofue 2015 halo surface mass density; the *red solid curve* is the corresponding DM2 disk density.

2.4. Mass–Luminosity Analysis

To qualify the computed surface mass density in the context of dark matter investigations, we analyze density profiles in conjunction with corresponding observed surface brightness profiles.

For each radial point of a galactic disk, we divide the corresponding local density by local brightness to obtain the local mass-to-light (M/L) ratio. For each galaxy, a set of all M/L values along the disk radius comprises its radial M/L profile. The numerator in these M/L ratios represents all matter, including stars, substellar objects, stellar remnants, gas, etc. However, we deliberately and conservatively treat *all* mass as stars, thinking of total M/L profiles as if they were *stellar* M/L profiles.

The reason for such treatment of M/L profiles is two-fold. First, prosaically, there are no accurate observational data on the radial distribution of non-stellar material in galaxies: It is impossible to reliably adjust galactic total density by subtracting non-stellar density. Second, beneficially, we can make use of the empirical mass–luminosity relation (MLR) of main-sequence stars to infer, from each radial M/L value (local density/brightness ratio), a corresponding main-sequence star with a unique combination of mass and luminosity. We refer to such star as *the characteristic star* and compute characteristic star mass for each radial datapoint of each galaxy in our sample, using the following logic and procedures.

Considering that the empirical scaling relation between main-sequence star mass and luminosity is given by power-law function $L = a\mathrm{M}^b$, where M and L are in units of solar luminosity ($L_\odot$) and solar mass ($\mathrm{M}_\odot$), respectively, we can express star mass as a function of its mass/luminosity ratio:

$$\mathrm{M} = (a\ \mathrm{M}/L)^{1/(1-b)} \quad (3)$$

In this form, given coefficients a and b[4], the formula can be used to compute characteristic star mass $\overline{\mathrm{M}}$ for a locale with known surface mass density $\Sigma(r)$ and surface brightness $S(r)$:

$$\overline{\mathrm{M}} = (a\ \Sigma/S)^{1/(1-b)} \quad (4)$$

[3] Halo mass within a cylinder of radius *r* should not be confused with mass within a sphere of radius *r* [33].

[4] See Appendix B for details on stellar MLR coefficients.

The application of this procedure to all pairs of $\Sigma(r)$ and $S(r)$ yields the galactic *radial profile of characteristic star mass*. We use this idealized stellar population fitting to check compliance of each $\Sigma(r)/S(r)$ pair with the limits of main-sequence MLR[5].

As the M/L ratio tends to increase in galaxies towards the periphery (causing characteristic star mass to decline radially), and considering that we implicitly include non-stellar matter in M/L analysis, the above procedure may encounter unphysical values of $\overline{M} < 0.075\ M_{\odot}$ (below the minimal star mass limit). At these occurrences, the bottleneck is surface brightness $S(r)$, and so we tentatively assume:

$$\overline{N}_{\text{min stars}} = S/L_{\text{min star}} \quad (5)$$

where $\overline{N}_{\text{min stars}}$ is such count of smallest red dwarf stars that would match the value of the observed surface brightness if the local stellar population consisted of lowest-mass stars; and $L_{\text{min star}}$ is the luminosity of a minimal red dwarf estimated as $L = a(0.075\ M_{\odot})^{b}$, with a and b calibrated for the very tip of the Main Sequence as per Appendix B.

This theoretical count of minimal stars allows to calculate the *excess surface mass density* (also referred to here as excess density) which represents the difference between the total density and the light-constrained maximum stellar density for a given level of surface brightness:

$$\Sigma_{ex}(r) = \Sigma(r) - 0.075\ M_{\odot} \times \overline{N}_{\text{min stars}} \quad (6)$$

We compute radial profiles of characteristic star mass and radial profiles of excess density for each galaxy in our sample and then aggregate individual galaxy findings and explore general sample-level trends, which we present in Section 4.

2.5. Further Analysis

It is not always possible to perform M/L analysis out to the edge of RC. There are cases where pairwise density/brightness matching halts around the radius where the brightness profile is truncated by the limiting magnitude of a telescope, with density profile carrying on towards galactic periphery alone. In such a situation, one can only study surface mass density. Accordingly, we assess dynamics between the peak value of excess density and the total density at the end of a rotation curve, both for individual galaxies and groups.

2.6. Conclusions Regarding Dark Matter

For each galaxy in our sample, as well as for sample-level "average galaxy", we study the radial profiles of the two above-defined metrics, characteristic star mass and excess density. For galaxies where characteristic star mass always stays above the minimal star mass limit (and hence no excess density is observed), we conclude *that no dark matter is required at all within the density/brightness observational radii* to explain empirical observations of rotation and luminosity.

The rationale for such a conclusion is that the combination of total surface mass density and surface brightness at all radii can be explained, in principle, by fitting a main-sequence stellar population. Naturally, such stellar population will exhibit a radially declining star mass gradient. We believe this is a norm, rather than an oddity, and put forward a *testable hypothesis that average star mass tends to decline along a galactocentric radius*. Considerations about the declining radial star mass gradient and references to relevant empirical evidence are provided in Section 5.

For galaxies exhibiting non-zero excess density, we check whether these values are within plausible estimates of non-stellar baryonic mass and/or whether they can be explained by other ordinary factors such as visibility cutoffs and uncertainty of empirical data. We discuss and attempt to quantify some of these factors in Section 5. We consider that galaxies where average computed excess density is below an ordinarily explainable level (adopted at 20 $M_{\odot}/pc^{2}$) require no dark matter.

---

[5] This procedure shall not be used to find exact populations which must additionally obey observed metallicity and other physical properties, and where Σ(r) must exclude non-stellar matter.

2.7. Summary of the Analytical Framework

Here we summarize the logical sequence discussed above. We start with an observed galactic rotation curve which we convert into a radial density profile (using DM2 model based on two key assumptions: thin disk, Newtonian physics). We then divide each datapoint of the surface mass density profile by a corresponding datapoint of the observed surface brightness profile, to produce the radial M/L profile of the galaxy. Assuming that all galactic mass is in stars, we use empirical main-sequence stellar MLR to convert each datapoint of the radial M/L profile into a characteristic star mass, thus obtaining the radial distribution of characteristic star mass. If all datapoints of the characteristic star mass profile contain a physically plausible value (> 0.075 $M_{\odot}$), we conclude that no dark matter is required within the density/brightness observational radius. If some of the characteristic star masses fall below the minimum mass limit, we compute the corresponding value of excess density. If all excess density points can be explained with ordinary factors, we conclude that no dark matter is required within the density/brightness observational radius. To the extent there are excess density datapoints which cannot be fully explained with ordinary factors, we conclude that further checks are needed. Figure 3 recaps the key points of our analytical framework in a flowchart format.

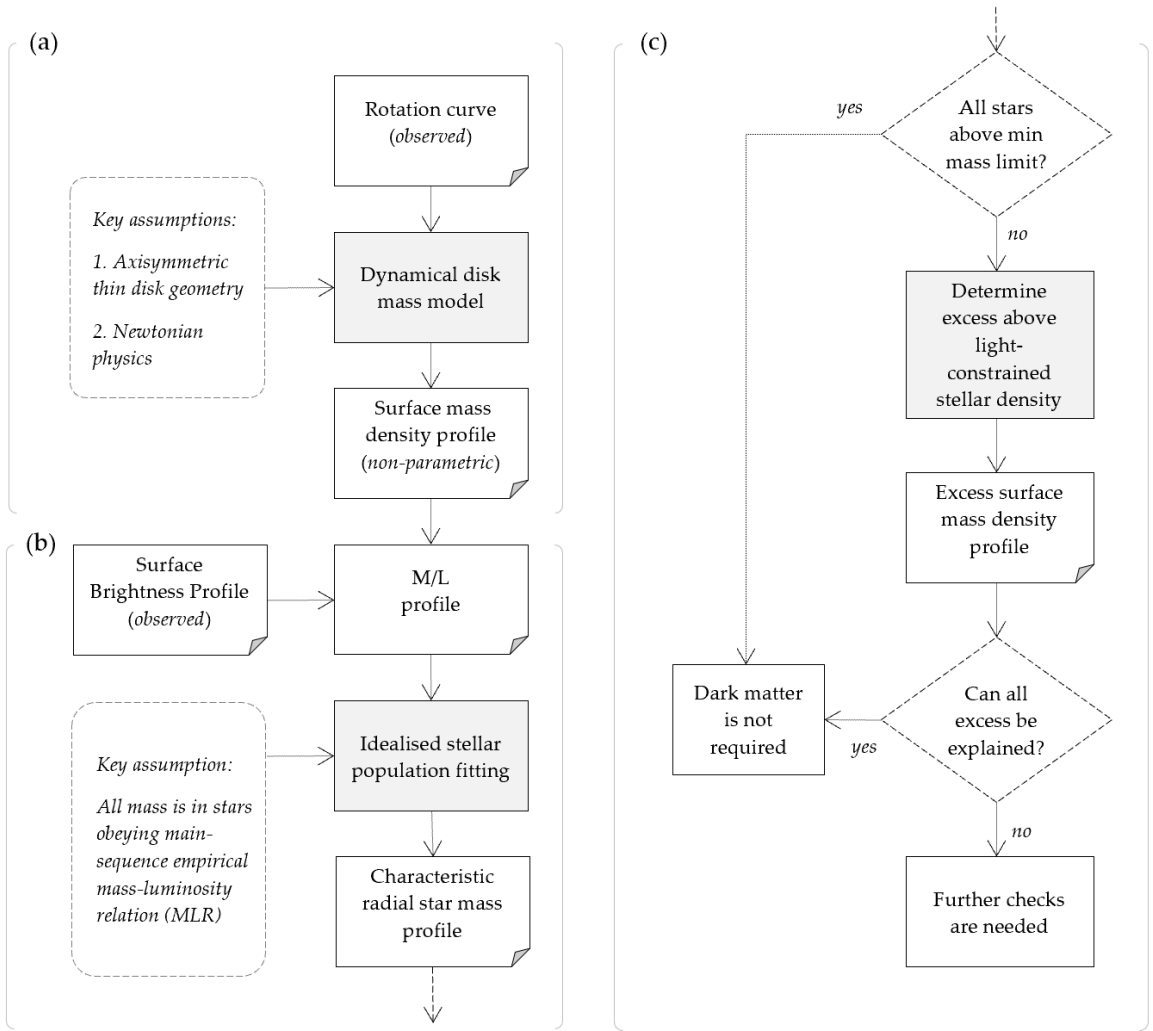

Figure 3. Outline of our analytical framework. Part (**a**) shows that galactic density profiles are derived from empirical rotation curves using our DM2 mass model. Part (**b**) shows that galactic surface mass density profiles and surface brightness profiles are then used to derive radial mass-to-light (M/L) profiles and characteristic star mass profiles. Part (**c**) shows the logic of analytical procedures applied to the results of Part (b) to arrive at conclusions about dark matter.

3. Data Sample

We assembled a dataset of 214 galaxies covering a broad range of sizes, heliocentric distances, morphologies, luminosities, and rotation velocities (see Appendix E). Figure 4 provides a snapshot of the sample along with correlations between these general properties. Consistent with other studies [35,36], our sample exhibits tight Tully–Fisher relation (correlation of peak rotational velocities with total galactic 3.6 μm luminosities is >0.8[6]), as well as other well-known correlations.

To make galaxies of a different size comparable, we express their radii in units that are multiples of R_{27}—the radius at which 3.6 μm apparent surface brightness reaches 27 $mag_{AB}/arcsec^2$. R_{27} marks the area within which Spitzer IRAC Channel 1 sensitivity stays relatively high, and is a useful common basis for comparing galaxies.

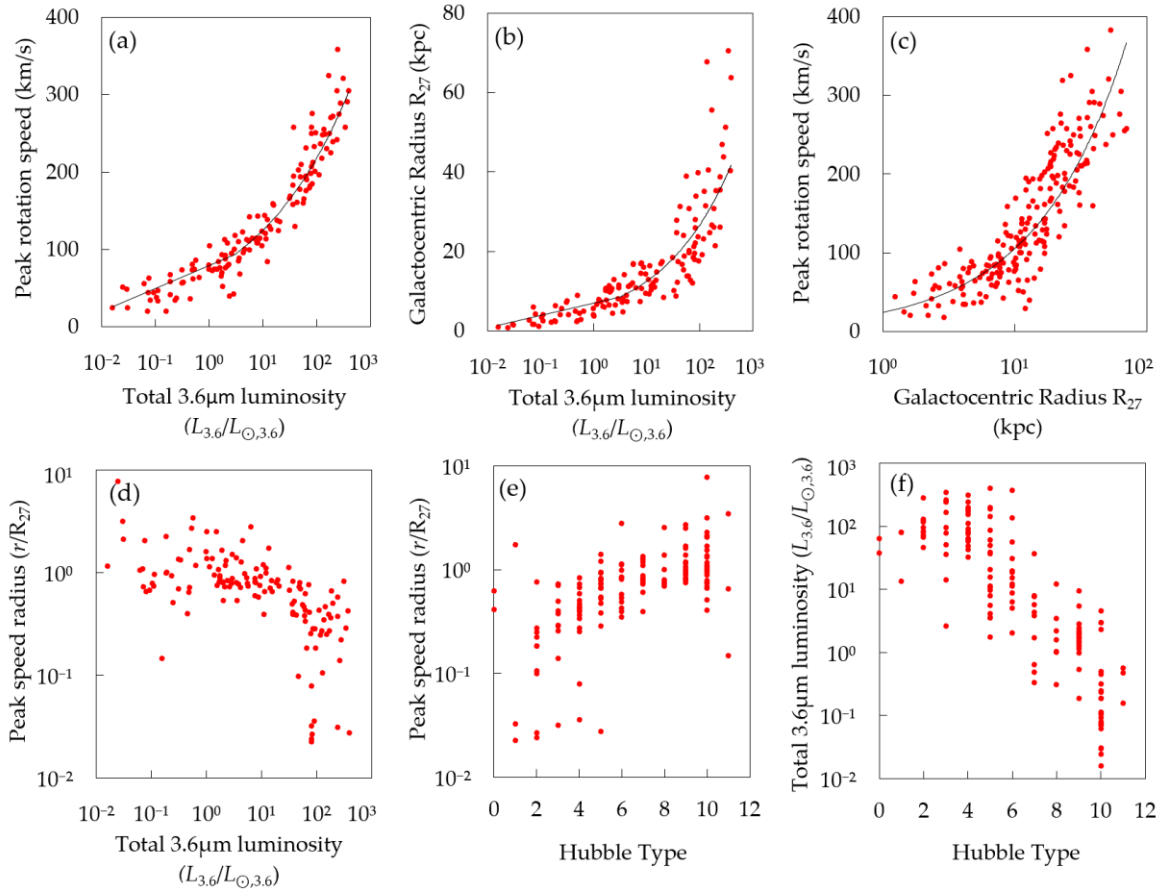

Figure 4. Summary statistics for 214 galaxies: (**a**) Peak rotation velocity vs. total 3.6 μm luminosity; (**b**) R_{27} vs. total 3.6 μm luminosity; (**c**) peak rotation velocity vs. R_{27}; (**d**) radial position of peak rotation velocity vs. total 3.6 μm luminosity; (**e**) radial position of peak rotation velocity vs. Hubble type; (**f**) total 3.6 μm luminosity vs. Hubble type. Luminosity values are shown in 3.6 μm solar luminosity units. R_{27} is the radius at which 3.6 μm apparent surface brightness fades to 27 $mag_{AB}/arcsec^2$. *Red-filled circles* represent individual galaxies.

For each galaxy, our dataset includes two major components: A Spitzer IRAC channel 1 surface brightness profile (3.6 μm) and a rotation curve. Sixty-nine percent of brightness data were obtained from The Spitzer Survey of Stellar Structure in Galaxies (S4G) [37–40] and 31% from the SPARC database [35]. Appendix C details our surface brightness data processing, which included unit conversion from $mag_{AB}/arcsec^2$ to $L_{\odot,3.6}/pc^2$, data cleaning, and inclination adjustments. Figure 5 shows all 214 inclination-corrected surface brightness profiles superimposed.

[6] This fact alone is a strong argument against dark matter. Galactic rotation *is* shaped by ordinary baryons.

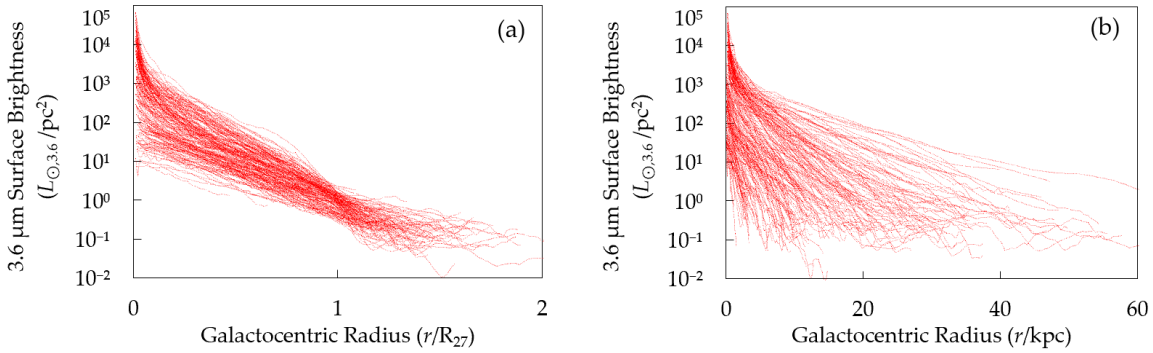

Figure 5. Spitzer 3.6 μm surface brightness profiles of 214 galaxies: (**a**) Plotted for ease of comparison against radii rescaled as multiples of R_{27}, the latter is determined empirically for each galaxy as the radius at which 3.6 μm apparent surface brightness fades to 27 mag_{AB}/arcsec^2; (**b**) plotted against radii in kpc.

Given the absence of extensive RC databases, we collected rotation data piecemeal from various sources ranging from RCs of individual galaxies to aggregated datasets. In particular, we greatly benefited from THINGS [36,41], GHASP [42,43], and SPARC databases, professor Yoshiaki Sofue's papers [11,44,45], as well as Swaters et al. [46]. One hundred and fifty-six RCs in our sample came from a single source and were adopted "as is". For the remaining 58 galaxies, where RCs were available from multiple sources, we created composite RCs following the procedure outlined in Appendix D. All RCs are superimposed in Figure 6.

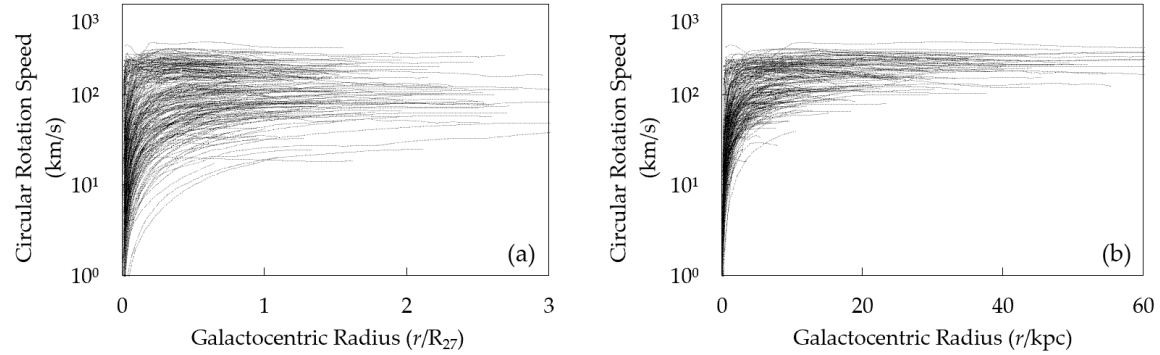

Figure 6. Superimposed 214 rotation curves: (**a**) Plotted against radii expressed in r/R_{27} units; (**b**) plotted against radii expressed in r/kpc units. The Y-axis log scale shows rotation speed in km/s.

Lastly, we used NASA Extragalactic Database (NED) and HyperLeda Database as a crosscheck for morphologies, inclinations, and heliocentric distances, and compiled a set of physical parameters of 724 main-sequence stars to calibrate empirical stellar mass–luminosity relation (MLR) function for Spitzer 3.6 μm passband (see Appendix B).

4. Results

4.1. Statistical Summary

For 132 or 62% of the galaxies in our sample, the entire M/L profile can be fully explained by a radially declining star mass gradient. Although M/L profiles of the remaining 82 galaxies cannot be completely addressed by an idealized stellar population fitting, the average excess density in these

galaxies is merely 14 $M_{\odot}/pc^2$, hardly sufficient to invoke dark matter[7] (Figure 7). Even a more conservative average of just peak excess densities is only 18 $M_{\odot}/pc^2$. Moreover, in most galaxies, these peaks are around r~1.1 R_{27}, declining thereafter. Many of these excess density values are at the cusp of Spitzer telescope visibility for red dwarf stellar populations and comparable with likely densities of gas and other low-luminosity baryonic matter.

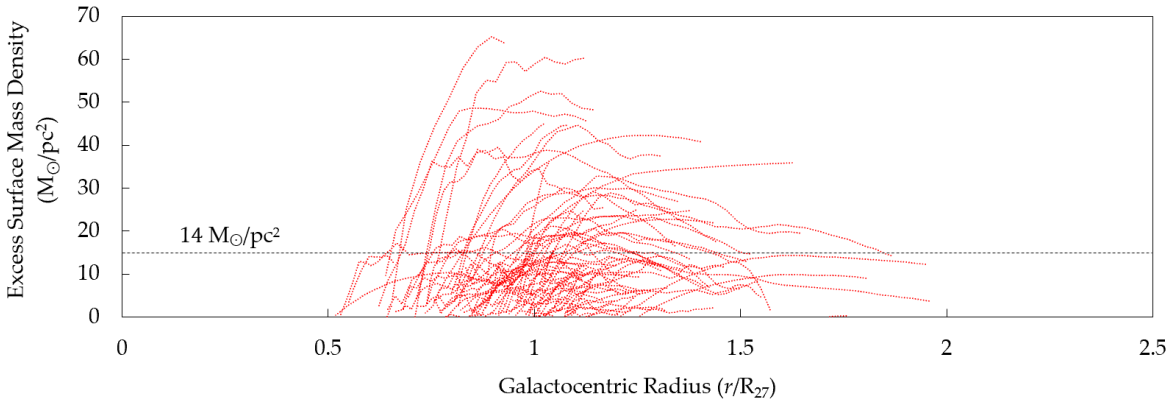

Figure 7. Superimposed excess density profiles are shown as *red thin curves* for 82 galaxies whose radial M/L profile cannot be fully explained by radially declining star mass gradient; 14 $M_{\odot}/pc^2$ is the mean average of all $\Sigma_{ex}(r)$ datapoints. The X-axis is a galactocentric radius in units of r/R_{27}.

Charts below (Figure 8) illustrate surface mass density profiles superimposed with surface brightness profiles for 214 galaxies, as well as basic mass–luminosity analytics, including brightness/density correlations, M/L profiles, and characteristic star mass profiles.

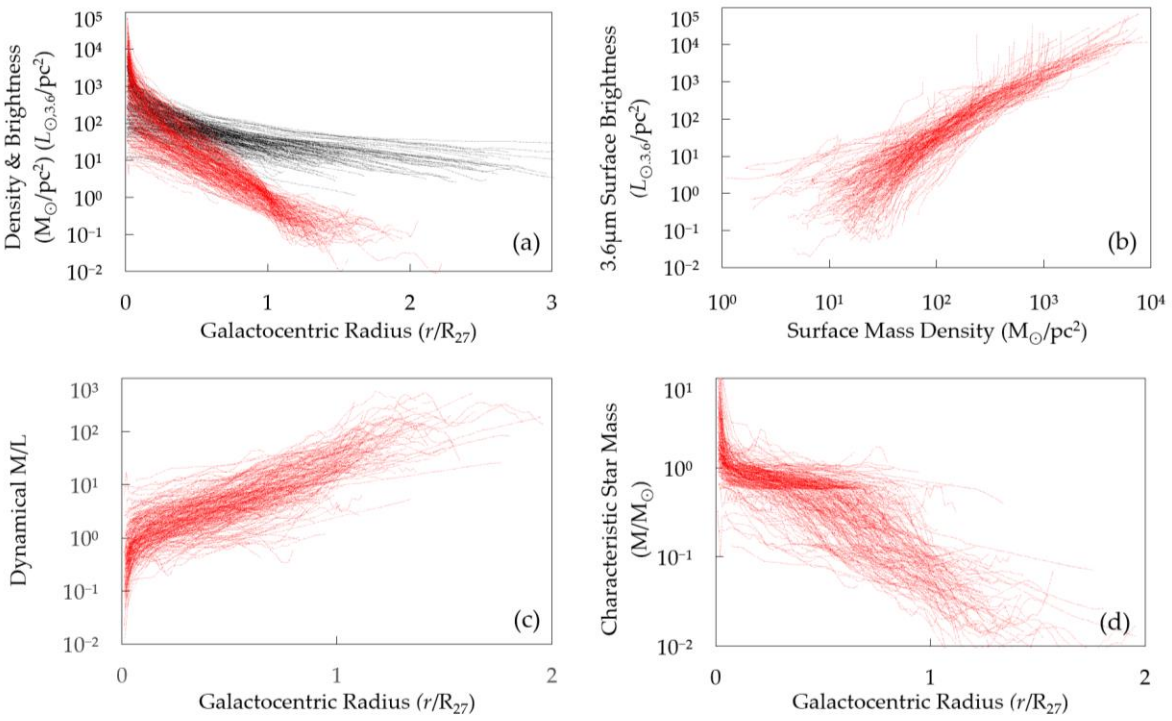

Figure 8. Illustration of mass–luminosity analytics for 214 galaxies. (**a**) Surface mass density profiles computed from individual galaxy rotation curves using DM2 model (*black curves*) superimposed with Spitzer 3.6 μm inclination-corrected surface brightness profiles (*red curves*); (**b**) correlation between

[7] For 15 out 82 galaxies, average excess density is above 20 $M_{\odot}/pc^2$, requiring additional data checks.

density and brightness datapoints; (**c**) rolling M/L profiles; (**d**) radial profiles of characteristic star mass.

Figure 9 presents *sample-level radial trends* of the same metrics as shown in Figure 8. Individual profiles of 214 galaxies were cut into radial bins, each with a width of 0.01 R_{27}; and average values of density and brightness were computed for each bin (mean average of all datapoints falling into a bin). The resulting compressed profiles represent average density and brightness trends across our galaxy sample on the r/R_{27} radial scale.

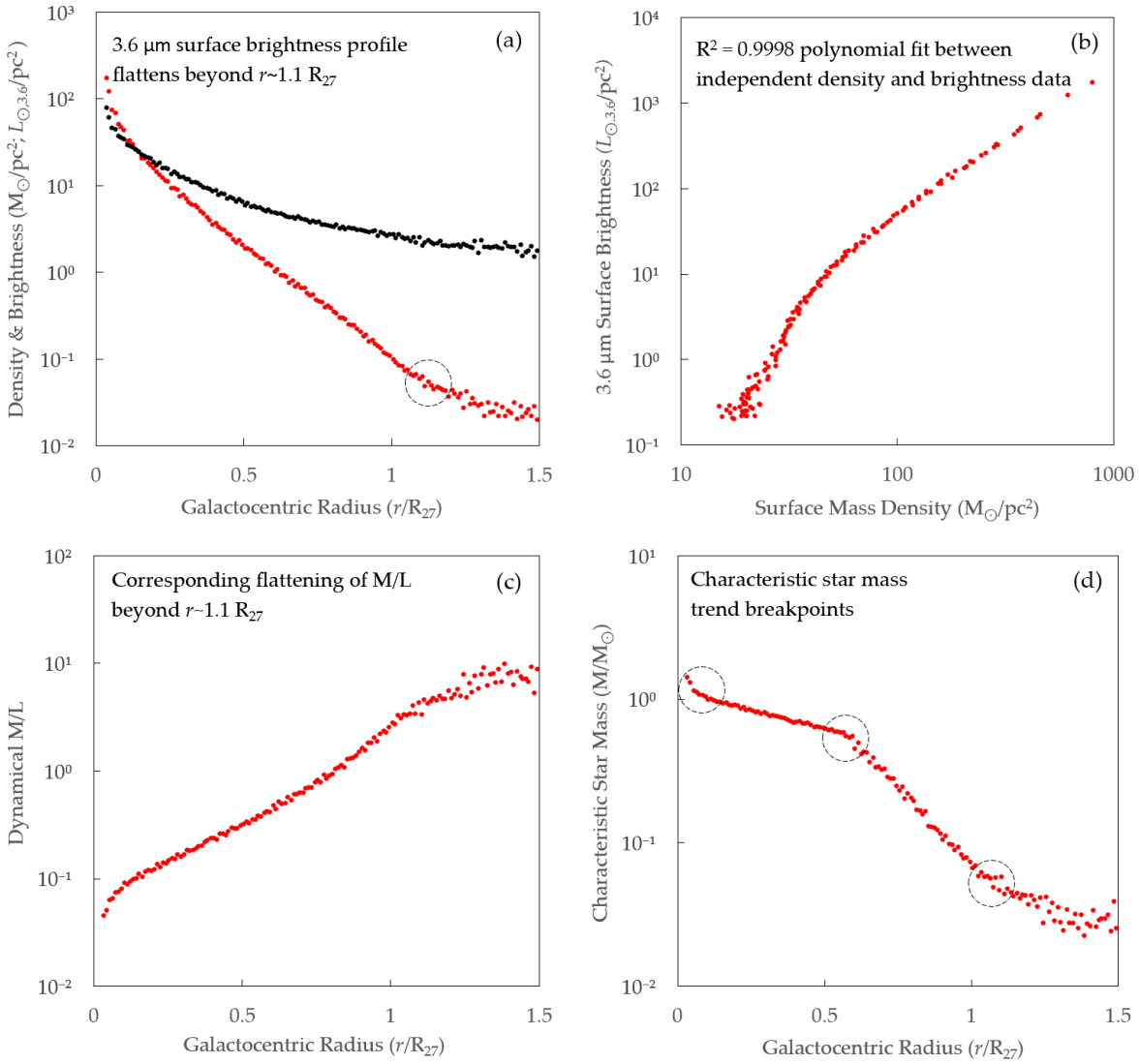

Figure 9. Sample-level radial trends in (**a**) surface mass density $\Sigma(r)$, shown in *black*, and surface brightness $S(r)$ shown in *red*; (**b**) correlation between $\Sigma(r)$ and $S(r)$; (**c**) M/L ratio; (**d**) characteristic star mass profile. Each circle represents a mean average value across all datapoints of 214 galaxies, which fall into a radially corresponding bin of 0.01 R_{27} width.

Before we proceed with the analysis of Figure 9 trends, we remind that the density and brightness data in our sample are independent data series. The former was computed using the DM2 model, exclusively from RCs (see source info in Appendix F), without any additional data inputs. The brightness is completely unrelated data from S4G and SPARC, and our galaxy sample is highly diversified in terms of morphologies, sizes, inclinations, etc.

Figure 9a shows sample-level radial trends in density and brightness. Whilst diverging initially to ~2 dex vertical gap, the two profiles flat out notably at r~1.1–1.3 R_{27}. This gearshift in density–brightness interplay is a likely reason for excess density $\Sigma_{ex}(r)$ peaking around the r~1.1 R_{27}

breakpoint in most galaxies. This existence of such inflection point, if confirmed on wider datasets with higher quality photometry, will have profound consequences for dark matter hypothesis, as the automatic assumption that light intensity necessarily continues to decline considerably faster than mass density *at all radii*, will be invalidated. We believe that the reason this breakpoint has not been reported earlier might be that large galaxy samples have not been scrutinized the way we propose in this paper, namely: Empirical-only (without extrapolations) light radially bin-averaged on r/R_{27} scale for a sufficiently large and diversified set of galaxies. Unfortunately, the current limitations of instruments make post-R_{27} surface brightness data scarce and barely reliable, but next-generation telescopes will be capable to definitively confirm or disprove this breakpoint and the flattening of surface brightness profile tails.

Figure 9b shows something even more interesting—an incredibly tight sample-level radial correlation between the 3.6 μm surface brightness and the dynamical surface mass density. Polynomial curve fits for brightness as a function of density achieve R-squared of 0.9998. If one increases the radial bin width when averaging density and brightness across the sample, and excludes the noisy post-R_{27} data, the already amazing correlation between the two independent data series (average density and brightness profiles of an eclectic ensemble of 214 different galaxies) becomes even stronger.

To round off the sample-level results, we review the M/L profile and the characteristic star mass profile (Figure 9c and 9d, respectively). As expected, the M/L ratio is gradually increasing as a function of radius, but it remains compliant with empirical stellar mass-luminosity relation (Appendix B) until r~1 R_{27}, beyond which excess density becomes non-zero. The growth of the M/L ratio is very smooth. This picture is echoed in the radial profile of characteristic star mass, which gradually declines with radius, in accordance with our hypothesis that the average star mass tends to decline as one proceeds from the center towards galactic periphery. The profile has visible breakpoints, which can be compared with the breakpoints in main-sequence stellar MLR (see Appendix B). The last breakpoint (at r~1 R_{27}) marks the start of the "sub-stellar" zone where the characteristic star mass slips below 0.075 $M_{\odot}$ and excess density starts to show, reaching a ~14 $M_{\odot}/pc^2$ peak before starting to descend. The gap between the total dynamical density and the excess density narrows to ~33% around r ~1.5 R_{27}, with $\Sigma_{ex}(1.5\ R_{27})$~11.1 $M_{\odot}/pc^2$ and $\Sigma(1.5\ R_{27})$~16.7 $M_{\odot}/pc^2$). By r~1.9 R_{27}, excess density declines to ~8.2 $M_{\odot}/pc^2$, which is 14% below the corresponding value of total density (~9.6 $M_{\odot}/pc^2$).

All contemporary surface brightness-related metrics, including our estimates of excess density, must be taken with a grain of salt for $r >> R_{27}$ due to higher uncertainties in light data beyond the 27 $mag_{AB}/arcsec^2$ level of 3.6 μm surface brightness. Nevertheless, we think that the above measurements and computed values are good first approximations that can be used to evaluate overall M/L trends in galaxies.

4.2. Representative Galaxies

To offer a more granular view at the level of individual galaxies, Figure 10 displays six representative specimens out of 132 galaxies without any excess density as per our M/L analysis. These six galaxies have a broad range of sizes, morphologies, velocities, distances, and inclinations, but all are explainable with radially declining star mass hypothesis. NGC2998 and NGC4303 have both RCs and surface brightness profiles longer than R_{27}, which makes successful stellar fitting along the whole length of RC even more remarkable. Not only all six galaxies do not require any dark matter within observational radii where both density and brightness data are available, but with their low peripheral density, dark matter can be ruled out even if respective RCs are extended with future measurements.

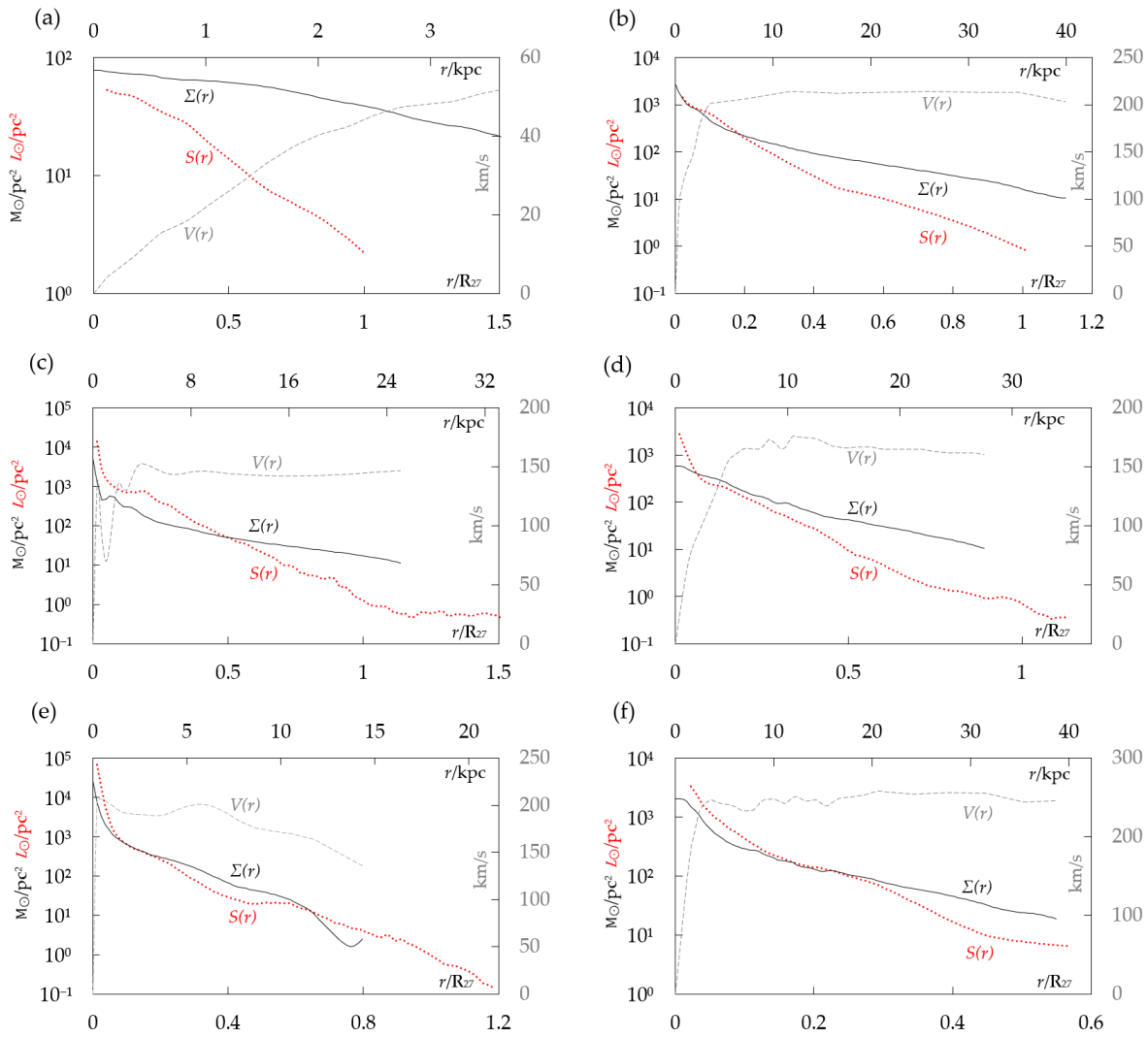

Figure 10. Representative cases from a 132-strong subsample of galaxies which do not show any excess density within observational radii: (**a**) NGC2366; (**b**) NGC2998; (**c**) NGC4303; (**d**) NGC1090; (**e**) NGC1808; (**f**) NGC6195. Twenty-five galaxies in this subsample have both RC and surface brightness profile length > R_{27}, while for the remaining 107 galaxies, either RC or surface brightness profile length is shorter than R_{27}. *Red and black curves* represent surface brightness *S(r)* in $L_{\odot,3.6}$/pc² and surface mass density in $M_\odot$/pc², respectively (*left side Y-axis*). The *dashed grey curve* is the rotation curve *V(r)* in km/s (*right side Y-axis*). *Lower X-axis* is in units of *r*/R_{27}. *Upper X-axis* is in units of *r*/kpc.

To provide a balanced and proportional illustration of our sample, Figure 11 shows four representative galaxies out of 82, the radial M/L profiles of which cannot be fully addressed by stellar MLR. For the first two examples—NGC5907 and NGC4157—peak excess density is under 15 $M_\odot$/pc², never quite approaching the total density curves and declining to 3.9 and 5.4 $M_\odot$/pc², respectively. We consider these and similar galaxies as benign cases, with hardly enough excess density and low total peripheral density to warrant dark matter speculation. Sixty-seven of 82 galaxies are like this, with average $\Sigma_{ex}(r) < 20$ $M_\odot$/pc² within observational radii. The third example, NGC0300, is one of the nearest galaxies in our sample at 2 kpc distance from the Sun and offers a peculiar case. Although its maximum $\Sigma_{ex}(r)$ is 28 $M_\odot$/pc², it traces total density downward slope to 10.9 $M_\odot$/pc² and then rapidly declines to 1.2 $M_\odot$/pc² matching a bounce in luminosity and reflecting sensitivity to the low light data, which could also be an error of measurement. Lastly, blue dwarf galaxy NGC2915 is our worst case with a maximum excess density of 65 $M_\odot$/pc² coming down to ≤10 $M_\odot$/pc² over a radial distance of ~2.6 R_{27}.

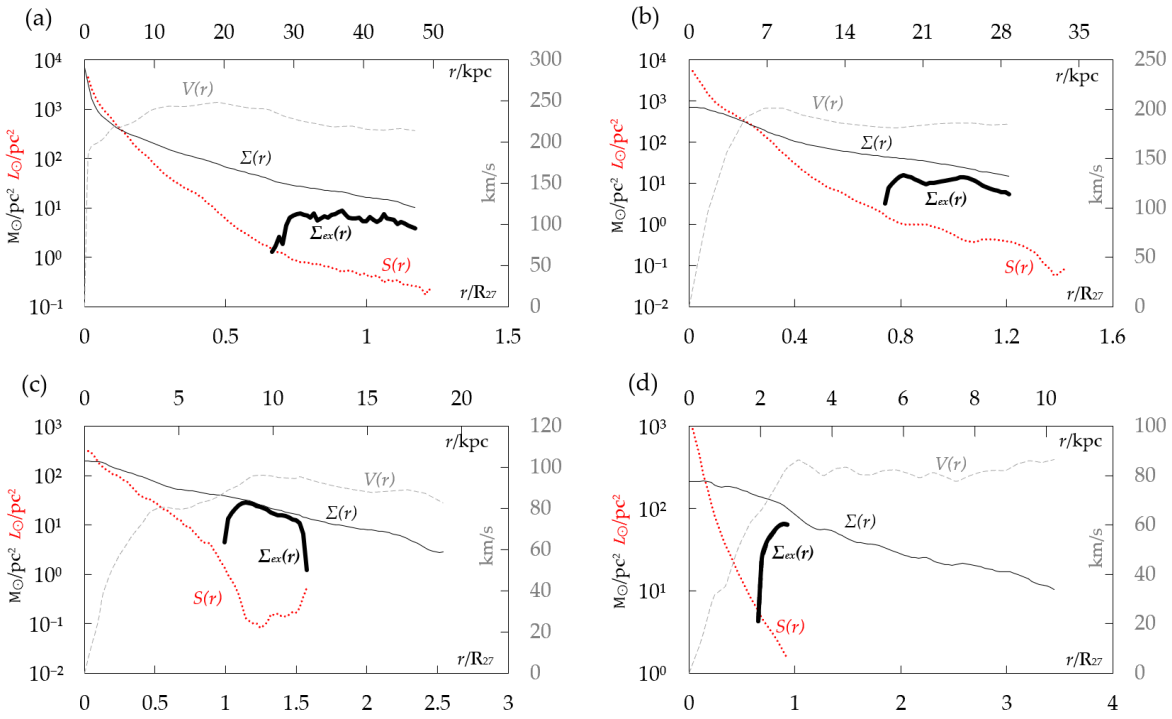

Figure 11. Representative cases for a subsample of 82 galaxies showing some excess density: (**a**) NGC5907; (**b**) NGC4157; (**c**) NGC0300; (**d**) NGC2915. *Red and black thin curves* represent surface brightness $S(r)$ in $L_{\odot,3.6}/pc^2$ and surface mass density $\sum_{(r)}$ in $M_\odot/pc^2$, respectively (*left side Y-axis*). The *Black thick curve* is density excess above light-constrained stellar density $\sum_{ex(r)}$ in $M_\odot/pc^2$ (*left side Y-axis*). The *dashed grey curve* is rotation curve $V(r)$ in km/s (*right side Y-axis*). *Lower X-axis* is a galactocentric radius in units of r/R_{27}. *Upper X-axis* is a galactocentric radius in units of r/kpc.

5. Discussion

The results presented in Section 4 rest on key assumptions that (a) all dynamical mass is in a disk, and that (b) stellar M/L varies with radius. Given this premise, the fact that for 132 galaxies or 62% of our sample the radial M/L profile can be explained solely by declining star mass gradient is a strong argument against dark matter.

We believe, furthermore, that most of the remaining cases can also be addressed without dark matter. Datapoints with non-zero excess density can be attributed to a *combination of several factors*—limits of light detection for red dwarf populations, the underestimated presence of low-luminosity baryonic mass, the uncertainty of distances, inclinations, rotation curves, and surface brightness data. Below we discuss these considerations and provide general observations on the dark matter hypothesis.

5.1. Limits of Detection of Red Dwarf Populations

The average S4G surface brightness profile is stated to trace isophotes at μ3.6(AB)(1σ) ~27 mag/arcsec², which is stated to be equivalent to a stellar mass surface density of ~1 $M_\odot/pc^2$ [37]. Such a low surface density threshold is misleading. The 1 $M_\odot/pc^2$ interpretation is correct only for the stellar population including Sun-like or heavier stars. If one assumes a population of red dwarfs of masses approaching 0.075 $M_\odot$ (minimal star mass corresponding to the hydrogen-burning threshold), then Spitzer IRAC channel 1 sensitivity drops to ≈C × 40 $M_\odot/pc^2$, where C is inclination correction (Figure 12). Such a red dwarf population with a density below C × 40 $M_\odot/pc^2$ will likely appear noisy or indistinguishable from the background in Spitzer 3.6 μm filter. Forty percent of 82 galaxies have excess density datapoints below the visibility threshold for 0.075 $M_\odot$ stars.

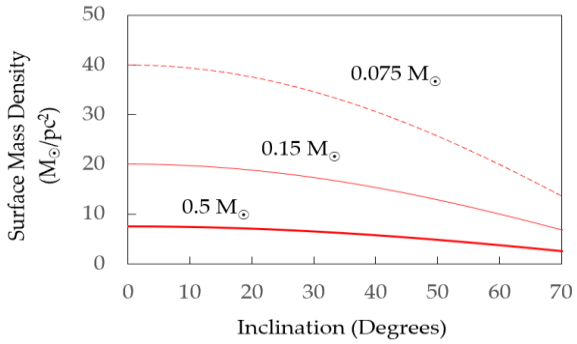

Figure 12. Approximate limits of Spitzer IRAC channel 1 detection (at 27 mag_{AB}/arcsec² apparent surface brightness) for stellar populations consisting exclusively of stars with masses 0.075 $M_{\odot}$, 0.15 $M_{\odot}$ or 0.5 $M_{\odot}$, expressed in terms of surface mass density ($M_{\odot}$/pc²). X-Axis shows inclination of galactic disk in degrees. Here, we assume inclination correction $C = \cos(i)$ and use our adopted main-sequence stellar MLR function estimated for Spitzer 3.6 μm passband (see Appendix B).

5.2. Low-Luminosity Baryonic Mass

Favoring a simpler approach in our mass–luminosity analysis, we ignored all low-luminosity baryonic mass such as gas, dust, brown dwarfs, etc. Estimates for these classes are often imprecise and, except for gas content, rarely provide radial distributions making it difficult to apply directly to the M/L problem. Table 1 provides the summary of contemporary research, as well as our attempt to quantify likely densities for different categories of baryonic matter assuming a total surface mass density of 27 $M_{\odot}$/pc², the average density for our sample at r~R_{27}.

Acknowledging a high degree of uncertainty, we believe that, in total, low-luminosity baryons could account for ~10 $M_{\odot}$/pc² as a first approximation estimate. This is probably a conservative number for several reasons. First, new findings, such as the discovery of massive HI medium enveloping M31 a thousand times larger than previously believed [47], consistently pushed these estimates upward, often by an order of magnitude, with the improvement of instruments and analytical techniques. Second, H_2 may be undetectable at lower abundances as there is not enough C and O present to give a signal [48]. Third, estimates for low-luminosity objects are based either on a limited sample set tied to particular locale (white dwarf census was just recently expanded from 20 to 40 pc around the Sun [49,50]) or on stellar evolution models backed by minimal empirical data (black holes, neutron stars). Fourth, brown dwarf frequencies are grounded in observations around the Sun and a few star-forming clusters, suggesting a ratio of 2–6 stars per brown dwarf. If our hypothesis of radially declining star mass gradient is valid, its logical extension is to expect a higher proportion of brown dwarfs in low-density galactic outskirts.

Table 1. Summary of contemporary estimates for various classes of low-luminosity baryonic mass. Estimates for brown dwarfs (BD), white dwarfs (WD), neutron stars (NS), and black holes (BH) assuming surface mass density ~27 $M_{\odot}$/pc², an average density across our sample at R_{27} (see Figure 11), and applying consistent global mass ratios to respective categories.

Category	Estimates	$M_{\odot}$/pc²
Gas (HI)	<10 $M_{\odot}$/pc² at R_{25} [51]	~6.0
Gas (H2)	<1 $M_{\odot}$/pc² at R_{25} [51]	~0.6
Gas (He)	He mass fraction Y_p=0.233 [52]	~2.0
Dust	Dust-to-gas ratio ~2 x 10^{-5} [53]	~0.001
Brown Dwarfs (BD)	10^{11} in Milky Way; >0.03 $M_{\odot}$ BD mass [54]	~0.7
White Dwarfs (WD)	232 WDs within 25 pc around Sun [55–57]; 0.6 $M_{\odot}$	~0.9
Neutron Stars (NS)	10^8–10^9 in Milky Way [58]; 1.4 $M_{\odot}$ NS mass	~0.3
Black Holes (BH)	10^8 in Milky Way; 10 $M_{\odot}$ BH mass [59]	~0.2
Total		~10.7

5.3. Uncertainty of Inclinations and Distances

Some of the variables critical for galaxy rotation and M/L problem admit a significant degree of uncertainty. Distances to galaxies, for example, are far from being resolved precisely. In our sample, 74 galaxies have the upper bound of distance estimates at least double of the lower bound number. Galactic inclinations also present several problems. Face-on galaxies are good for surface brightness data but unreliable for rotation curves. Vice versa, highly inclined galaxies are good for velocity measurements but questionable for surface brightness data. For some galaxies, inaccuracies in these key input parameters can drastically alter the results of their mass/luminosity analysis.

5.4. Uncertainty of RCs

RC measurements are uncertain, especially for warped and low-inclination disks. The methodology for averaging of approaching and receding side velocities is not standardized. Many RCs have very low resolution, with only a few datapoints. For multiple RCs, there are strong disagreements between authors. Appendix D shows an example of such RC disagreement.

5.5. Uncertainty of Surface Brightness Data

There is a significant variation in surface brightness estimates, typically caused by differences in equipment used and data processing methodology applied, especially in the case of warped disks and irregular galaxies. For some galaxies, there is up to an order of magnitude difference between S4G "fr" and "fx" series at some radii. As noted in Appendix C, in only 20% cases of the S4G-SPARC overlap set of light data, the total luminosity estimates by SPARC differ from those by S4G by less than 10%. In the most extreme case, the difference reaches 9 times. Another source of significant uncertainty is the choice of filters. We used 3.6 μm data, but some radiation sources shine much brighter in other passbands, giving higher $L_{\odot}/pc^2$ values. A truly unambiguous image of a galaxy is bolometric, but unfortunately, such data are not available for our sample.

5.6. Uncertainty of MLR Slope for Smallest Red Dwarfs

Given relatively few datapoints for the smallest red dwarfs at the very tip of the Main Sequence, we took a conservative approach and ignored a breakpoint in power-law MLR function around 0.1 $M_{\odot}$, below which the function changes slope. Were we to use just the seven lightest stars to compute the MLR function, the coefficients would have been $a = 4.1$ and $b = 2.84$, with $R^2 = 0.98$ (instead of the adopted $a = 0.82$, $b = 2.17$). The application of this alternative set of coefficients in our mass–light analysis would have further reduced average excess density as well as the number of "light-deficient" galaxies.

5.7. Light Extinction

We have not applied any extinction adjustment to surface brightness profiles in our sample. We believe the impact of internal extinction ranges from zero for face-on galaxies, to 0.25 mag for edge-on galaxies. This is probably a conservative estimate as even face-on galaxies are likely to have some internal light extinction. Moreover, light is lost both in the intergalactic medium and within Milky Way. Although the former is assumed to be almost transparent in Spitzer 3.6 μm, even minor light loss over intergalactic distances can be cumulatively significant. Overall, it seems probable that substantially higher extinction corrections are necessary to fully account for all light loss. A 0.25–0.5 mag correction would have reduced the number of "light deficiency" datapoints in our sample by 19%–38%.

5.8. Plateau in Surface Brightness Profiles beyond R_{27}

As shown in Section 4, we discovered an inflection point around r~1.1 R_{27} in our sample-level average surface brightness profile. Outside this radial point, the gap between density and brightness appears to be no longer expanding. This agrees well with and explains the fact that for most of the relatively "light-deficient" galaxies in our sample excess density peaks around r~1.1 R_{27}. Current

technological limitations make it hard to confirm empirically with high confidence the flattening of light profile beyond the identified inflection point. However, this is, in principle, a testable hypothesis, which can be another strong argument against dark matter.

5.9. Evidence for Radially Declining Star Mass

The ideal empirical test for our hypothesis of radially declining star mass gradient would be direct observation of star distributions in different galaxies. Unfortunately, present knowledge of such distribution is limited even for the Milky Way. Galactic O-Star Spectroscopic Survey (GOSSS) [60] identifies the 590 brightest O-Star systems within our galaxy. Most of the identified O-Stars are located within central I and IV quadrants [61], directionally supporting our thesis, but the study accounts only for 1% of estimated total 50,000 O-type systems in the galaxy. According to the authors of GOSSS though, over 90% of the hidden O-stars are also in the quadrants I and IV. There is also a growing body of evidence of top-heavy initial mass function in the Galactic center [62,63] and more generally with increasing density [64].

Concentration of heavy stars in the center is expected given the minimal density and mass of maternal molecular cloud required for star formation. Theoretical reasons suggest a minimum density of $(5 \pm 2) \times 10^3$ cm^{-3} [65] and cloud mass of 30 $M_\odot$ for the lowest star mass of 0.075 $M_\odot$ required by a hydrogen burning limit. This is consistent with the smallest known star-forming globules with the mass range of 5–50 $M_\odot$. The minimal mass of a maternal cloud required to form a heavy star is considerably higher. For an O-type star with mass >20 $M_\odot$ to form with 95% probability, the cloud should be approximately 7×10^4 $M_\odot$ [66,67]. In a typical galactic periphery, where surface density drops below 50 $M_\odot$/pc^2, such cloud has to vacuum all mass within ~1 million pc^3.

5.10. Evidence of Extended Stellar Disks Around Galaxies

Several recent papers provided independent evidence of extended stellar disks around galaxies. For example, an extremely faint, outer stellar disk is observed to 10 scale lengths in NGC 300 [68]. In our neighbor, M31 Andromeda, there is evidence for stellar outer disk substructure [69]. M33 is also suspected to have significant outer stellar disk [70]. In some galaxies, like NGC 4013, giant stellar tidal streams around the disk were confirmed [71]. With new-generation telescopes, we expect the evidence for extended stellar disks to increase dramatically.

5.11. Strong Correlations between Dynamics and Light

Even without modelling density and auditing every radial M/L datapoint for compliance with stellar MLR (89% of the all density/brightness datapoints in our sample do pass the test), it is strikingly apparent from simple correlation analysis of basic properties for our 214 galaxies, that galactic rotation is shaped by baryons. As mentioned in passing in Section 3, the Tully–Fisher relation is confirmed with 0.83 correlation between total luminosity and peak rotational speed.

The Tully–Fisher relation is not the only confirmation that baryonic mass defines galactic dynamics. In Section 4, we presented sample-level radial mass–luminosity trends. Unlike Tully–Fisher, we do not compress a galaxy into a pair of numbers to then compare a group of galaxies. Instead, we squeeze together radial profiles of a large group of galaxies and look at general patterns *inside* an averaged galaxy. This inner perspective allows to see things impossible with Tully–Fisher analytics, such as the correspondence between density and brightness at different radii. Our approach and Tully–Fisher complement each other and jointly offer a strong argument against the idea of dynamically dominant non-baryonic dark matter. As showed in this paper, sample-level average galactic density profile correlates extremely with galactic light ($R^2 = 0.9998$) at all radii[8]. Furthermore, the density is *dynamically sufficient*. Therefore, the pro-dark matter interpretation, which is usually applied to Tully–Fisher relation (that baryonic matter must be correlated with dark matter), does not stand in the case of our analysis of galactic mass-luminosity trends.

[8] Excluding the centers of galaxies where super-massive objects and other factors complicate dynamics and the outskirts where stellar radiation signal-to-noise ratio is too low for modern equipment.

5.12. Lack of Evidence for Dark Matter in the Solar Neighborhood

It is unlikely for the Solar system to be in a dark matter-free bubble, if dark matter is as abundant in the universe as claimed. Considerable effort went into experiments attempting to detect weakly interacting massive particles [72,73], without any positive results. On the other hand, a study of surface mass density at the solar Galactocentric position between 1.5 and 4 kpc from the Galactic plane [74] accounted for visible mass only and compared expected and empirical kinematics of stellar objects. According to the authors, the visible mass strikingly matches the observations, presenting another empirical hurdle for the dark matter concept.

6. Conclusions

Using a diversified sample of 214 galaxies:

- We have demonstrated that all types of galactic rotation curves can be precisely tracked by a non-parametric disk model which requires lower surface mass density than estimated with parametric models with a dark matter halo.
- We have showed that in 132 galaxies, all radially corresponding density/brightness datapoint pairs within observational radii can be addressed solely by the assumption of radially declining average star mass[9].
- We have discussed how the average excess density of 14 $M_{\odot}/pc^2$ in the remaining 82 galaxies can be explained without appealing to non-baryonic dark matter, but instead with a combination of factors such as visibility cutoffs for dim stellar populations, the quality of various estimates, incompleteness of light data, and the low-luminosity baryonic content.
- We have presented an empirically testable hypothesis that radially rising mass/luminosity profiles might be a natural outcome of radially declining average star mass in galaxies.
- We have reported a finding of 3.6 μm galactic surface brightness profiles flattening beyond the r~1.1 R_{27} inflection point.
- Lastly, we have demonstrated the extremely tight correlation between sample-average radial profiles of dynamical mass density and surface brightness, with polynomial fit $R^2 \approx 1$.

For an unbiased rational thinker abiding by the Occam's razor principle, our analysis suggests that the widely popular and yet hopelessly theoretical dark matter must be rejected in favor of a simpler explanation. Perhaps dark matter is like Confucius' black cat—hard to find in a dark room, especially if there is no cat.

Author Contributions: Both authors were equally involved in all aspects of this project from conceptualization and methodology to analysis and writing. All authors have read and agree to the published version of the manuscript.

Funding: This research received no external funding.

Acknowledgments: We credit Konstantin Pavlovich for inventing original computational technique for galactic density profiles which became the basis of our DM2 method, and for inspiring us to research the problem of the galaxy rotation and dark matter in general. We thank Jouni Kainulainen and Christoph Federrath for kindly explaining their work on star formation. We also thank Jezus Maíz Apellániz for answering our questions on O-stars empirical distribution. Furthermore, this article would be impossible without data diligently compiled over the years by many people. We are especially indebted to Yoshiaki Sofue, THINGS and SPARC teams for compiling their RC databases, and S4G team for the extensive collection of galactic surface brightness profiles. Lastly, but most importantly, we want to express our gratitude to Anne M. Hofmeister for reaching out and arranging the "Debate on the Physics of Galactic Rotation and the Existence of Dark Matter".

Conflicts of Interest: The authors declare no conflict of interest.

[9] 89% of all density/brightness datapoints in our sample are in compliance with main-sequence stellar MLR.

Appendix A. Disk Mass Density Model (DM2)

DM2 is designed to infer, non-parametrically, the density profile of a galaxy from its rotation curve as the sole input into the model, using Newtonian gravitation as the operator linking mass and dynamics. The model can also be used in reverse mode, to compute the rotation curve corresponding to a given density distribution.

In DM2, a galaxy is approximated with an idealized, rotation-supported, ultrathin, axisymmetric, finite disk with a stable structure globally controlled by Newtonian equilibrium.[10,11] All matter rotates circularly in the plane of the disk. The disk is completely self-gravitating, not immersed in a dominating dark matter medium, and is not engaged in external interactions.

For a disk setup, we use polar coordinates (r, θ), where r is the radial distance from the origin and θ is a counterclockwise angle from the zeroth azimuth.

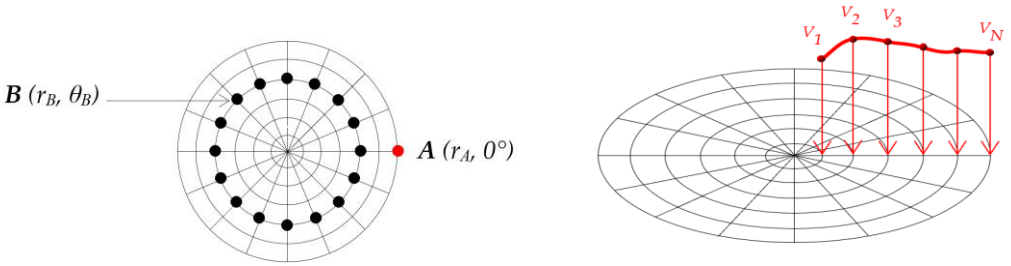

(**a**) (**b**)

Figure A1. (**a**) Illustration of disk setup. Point A represents the center of a location at zeroth azimuth ($\theta = 0°$) and radius r_A. Point B represents the center of a location at radius r_B and azimuthal angle θ_B. The polar coordinates of points A and B are (r_A, $0°$) and (r_B, θ_B), respectively. (**b**) Illustration of DM2 input. RC values are used to set model orbits.

The disk consists of N nested concentric and equidistant circular orbits, each consisting of P locations (each represented by a point), each pair of locations separated by a $2\pi/P$ angle. Due to symmetry, all locations on the same orbit are assumed to contain similar mass, characteristic for the orbit. At each orbit, the characteristic rotation speed is constant. Table A1 defines DM2 notations.

Table A1. Notations used in DM2 model formalism.

DM2 Notation	Definition
A (r_A, 0°)	A location centered at the intersection of orbit r_A and zeroth azimuth
B (r_B, θ_B)	Any other location, centered at the intersection of orbit r_B and azimuth θ_B
N	Number of modeled orbits in the disk plane (N+1, including the center)
P	Number of modeled locations in each orbit
V_A	Rotational speed at location A

[10] We acknowledge the existence of disk stability argument but do not find it convincing. We believe that conclusions about disk stability based on physics of fluids/gases or dynamical N-body simulations will remain tentative until computational power permits dynamical galaxy simulations of true scale and complexity. Modelling limitations shall not be used to shift responsibility for disk stability to hypothetical dark matter halos.

[11] The thin disk approximation is justified given that scales in the disk plane are much greater than along z-axis, and vertical density distribution is typically narrow. Bulges and stellar halos can be accounted for by a higher surface mass density. We compared a thin disk- and a cylinder dynamical mass models of M31, both with r_{max} = 300 kpc and with non-parametrically computed radial distribution of density on the basis of the same rotation curve. Having assumed the cylinder height of 4 kpc and exponential density distribution along z-axis (with 400 pc scaleheight) for the cylinder model, we get <1% enclosed mass difference between the disk and cylinder beyond r = 109 kpc.

m_B	Mass at location B

Radius r_N of the outermost orbit in the initial disk setup corresponds to the radius of the last datapoint in the empirical rotation curve (RC), which is used as model input. Rotational velocities of at each orbit are taken or inferred from the RC (see Figure A1,b). Considering that all orbits are radially equidistant from each other, some input RCs might need to be rescaled to provide DM2 with a regular-step rotational speed array [V_1; V_2 … V_N]. When needed, such rescaling is done through linear interpolation between pairs of relevant RC datapoints.

Considering that DM2 is a numerical model, it is preferable to set the values of N and P as high as practically allowed by computational resources. In our implemented version of DM2, we set N = 1000 and P = 3600.

Radial distribution of radius-specific masses [m_1; m_2 … m_N] is unknown and represents the variable set which DM2 is solving for.

The logic of the solution is based on integrating gravitation across modelled locations and encoding the balance between the known rotation curve and the unknown mass distribution (or, in inverse mode, between the known mass distribution and the unknown rotation curve) in a simple linear system, as shown below.

The gravitational force acting upon on a *unit mass* at point A (r_A, 0°) due to any randomly chosen point B is given by Newton's classical law of universal gravitation:

$$F\ [per\ unit\ mass\ at\ point\ A]\ = G\ \frac{m_B}{r_A^2 - 2r_A r_B \cos\theta_B + r_B^2} \tag{A1}$$

where G is the universal gravitational constant, and the denominator is the squared distance between points A and B (see Figure A1,a) in polar coordinates. The centripetal component vector of gravitational force F (acting on unit mass at point A due to point B) is given by:

$$F_{centripetal}\ [per\ unit\ mass\ at\ point\ A] = G\ m_B\ \frac{r_A - r_B \cos\theta_B}{(r_A^2 - 2r_A r_B \cos\theta_B + r_B^2)^{3/2}} \tag{A2}$$

For a disk with uniform circular planar rotation at each orbit, the centripetal acceleration at point A is equivalent to the *cumulative* centripetal gravitational force exerted on mass at point A by mass at all other points of the disk.

We integrate numerically all centripetal force components over the entire disk area as follows:

$$\frac{V_A^2}{r_A} = \frac{G}{s^2}\sum_{r=1}^{N}\left(m_r \sum_{p=1}^{P}\frac{r_A - r\cos 2\pi p/P}{(r_A^2 - 2r_A r\cos 2\pi p/P + r^2)^{3/2}}\right) \tag{A3}$$

where s is a scaler relating DM2 dimensionless disk radius and the physical radius given by the input rotation curve in kpc. The only unknown variable in Equation (A3) is m_r, the array representing radius-specific masses [m_1; m_2 … m_N].

Given a rotation curve and the coordinates of all modelled locations, all known variables can be instantiated, and we can write down Equation (A3) for each of the N possible positions of r_A along the zeroth azimuth, and thus construct an N×N linear equation system.

It is convenient to represent the above linear system, consisting of N Equations (A3) instantiated for each of N circular orbits, in compact matrix notation:

$$y\ =\ G\ C\ x \tag{A4}$$

where y, in matrix terms, is a column vector of squared rotation velocities at different radii[12]; G is a constant; C is a spatial coefficients matrix; and x is a column vector of radius-specific masses [m_1; m_2 … m_N][13]. The solution is a straightforward matrix multiplication:

$$x = G\,C^{-1}\,y \quad \text{(A5)}$$

The final result is a strict and invariant algebraic solution. The output mass profile can be converted into a surface density profile and/or an enclosed total mass profile.

It is also possible to compute rotation curves from mass (or density) distributions, e.g. to check the accuracy of tracking the input RC. DM2 has been tested on a broad range of galaxies and in all cases the results provided ideal fits with original input RCs.

In practical implementation of DM2, the following aspects must be considered. Even though disk potential prevents disk RC from full converge with a Keplerian RC for another radial length beyond the disk edge, a naïve version of the model will underestimate mass at disk edge due to the finite nature of empirical RCs, resulting in downward-pointing tails of density profiles and total enclosed mass (<R) profiles. We address this issue by adding a flat extension to the empirical RC. To neutralize the truncation effects, it is sufficient to extend the original RC by 15%–20%. The output mass profile is then trimmed back to the original RC length. Another practical consideration is the proximity of points *A* and *B* in high-resolution implementations, which must be controlled to prevent singularity-like artefacts.

DM2 is best used for galaxies that are close to ideal—flat, symmetrical, non-interacting. RCs of warped, lopsided, irregular, interacting, or otherwise non-ideal galaxies usually misrepresent the true rotation pattern. When such RCs are fed into DM2, it will still track them with extremely high accuracy, but the resulting radial mass distribution profiles should be taken with a grain of salt. That said, DM2 can be used as a litmus test for the "irregularity" of a galaxy. For example, for interacting galaxies like NGC5194, it will deliver what seems to be a meaningless density profile, with negative density values because of the interacting companion NGC5195.

Appendix B. Stellar MLR Coefficients for 3.6 μm Passband

Here, we present our estimation of power-law coefficients for stellar mass–luminosity relation (MLR) in Spitzer IRAC channel 1 passband centered on 3.6 μm wavelength. MLR functions were calibrated on four published sets of stellar parameters (Eker et al. (2015) [75], Malkov (2007) [76], Mann et al. (2015) [77], Vitrichenko et al. (2007) [78]), which were collated into a composite sample covering 724 main-sequence stars with masses ranging 0.08 $M_\odot$ to 51 $M_\odot$.

Table A2. Four data sets of stellar properties were included in a composite sample used to estimate the generalized relation between a star's mass and bolometric luminosity. Each set provides a reference table of basic parameters including star mass, radius, effective surface temperature, bolometric luminosity, or flux.

Study	Mann et al. 2015	Eker et al. 2015	Malkov 2007	Vitrichenko et al. 2007
Stellar domain	M dwarfs	Intermediate mass stars		Massive stars
Stellar mass range	0.084 … 0.744	0.214 … 30.884	0.214 … 32.7	10 … 51
Sample size	183	203	271	67

Traditionally, stellar mass–luminosity relation is given in the form of piecewise power function defined for intervals of stellar mass:

[12] For clarity, in matrix algebra terms $y = v \otimes v$, an outer product of two instances of column vector v, each containing rotational velocity values from the RC.

[13] Even if $V_0 = 0$, it is possible to include central mass m_0 in the model either by excluding m_N or by resizing the linear system to $N + 1$ assuming $V_{N+1} = V_N$.

$$(L_*/L_\odot) = a\ (\mathrm{M}_*/\mathrm{M}_\odot)^b$$

$$\log(L_*/L_\odot) = \log(a) + b\ \log(\mathrm{M}_*/\mathrm{M}_\odot)$$

To statistically estimate a piecewise MLR function of this form, we first plotted bolometric luminosities against star masses, using a logarithmic scale for both variables, and qualitatively identified mass ranges where MLR appears to be stable. We identified four breakpoints (≈0.15 $M_\odot$, ≈0.6 $M_\odot$, ≈1.08 $M_\odot$, ≈2.3 $M_\odot$) defining six intervals of relatively stable MLR for stars with masses between 0.08 $M_\odot$ and 51 $M_\odot$. We considered another breakpoint ≈10 $M_\odot$ but scatter at the higher mass end would make it irrelevant. The lowest mass interval, with the higher bound at ≈0.15 $M_\odot$, included only 17 stars but given that it has a theoretical basis (relating to the increasing level of electron degeneracy contribution in very low mass stars [79,80]), we decided to keep the ≈0.15 $M_\odot$ breakpoint in our estimation of MLR trends.

We then modeled synthetic 3.6 μm luminosity for each star in the sample, making use of temperature and radius information. This was done in two steps. First, approximating a star with a blackbody, we computed 3.6 μm radiant flux density by integrating Plank function in spectral emittance form over Spitzer IRAC channel 1 passband:

$$S(\lambda) = \frac{2\pi hc^2}{\lambda^5}\frac{1}{e^{ch/\lambda kT} - 1}$$

where h is Planck's constant, k is Boltzmann constant, c is the speed of light, λ is the wavelength, and T is the absolute temperature in degrees Kelvin (see Table A3 for passband information and values of constants used in the integration).

Table A3. Values adopted for estimation of Spitzer 3.6 μm MLR coefficients.

Constant	Value	Units
Planck constant, h	6.62607×10^{-27}	erg s
Boltzmann constant, k	1.38065×10^{-16}	erg/K
Speed of light, c	2.99793×10^{10}	cm/s
Stefan-Boltzmann's constant, σ	5.67037×10^{-5}	erg/s^1 cm^2 K^4
Spitzer IRAC1 filter passband (response > 1%)	3.13129–3.96136	Mm
Solar temperature, $T_\odot$	5772	K
Solar radius, $R_\odot$	6.95658×10^{10}	Cm
Solar mass, $M_\odot$	1.98855×10^{33}	G
Distance to the Sun, $D_\odot$	4.84813×10^{-6}	Pc
Solar luminosity—3.6 μm passband, $L_{\odot 3.6}$	3.42851×10^{31}	erg/s
Solar radiant flux density—3.6 μm passband, $F_{\odot 3.6}$	5.63772×10^{8}	erg/s cm^2

Then, multiplying the radiant flux density of each star by the surface area of a sphere with the star's radius ($4\pi r^2$), we obtained 3.6 μm luminosity (in erg/s) for each star in the sample. We completed similar procedures for the Sun and obtained an estimate of solar 3.6 μm luminosity. Dividing each star's luminosity by solar luminosity, we obtained $L_{*3.6}/L_{\odot 3.6}$ values, which could be used for estimating 3.6 μm MLR scaling coefficients.

We plotted the modeled 3.6 μm luminosities against star masses taken from the composite calibrating sample (Figure A2) and made sure that all bolometric breakpoints remain reasonable in 3.6 μm passband.

Lastly, using least-squares regression, we estimated power function coefficients a and b for each mass interval. As can be seen from R-squared values in Table B3 and is visually apparent from Figure A2, there is greater scatter in higher mass stars MLR, while the relation is tighter towards the lower mass end.

Values of a and b coefficients listed in Table B3 were used for galactic our mass–luminosity analysis to determine radial distribution profiles of characteristic star mass and excess density.

Table A4. Estimated coefficients for stellar MLR ($L = aM^b$) in Spitzer 3.6 μm passband.

Star Mass Range	$a_{3.6}$	$b_{3.6}$	R^2	Datapoints
0.08 $M_\odot$ … 0.15 $M_\odot$	0.84	2.17	0.99	17
0.15 $M_\odot$ … 0.57 $M_\odot$	0.40	1.80	0.99	153
0.57 $M_\odot$ … 1.08 $M_\odot$	1.12	3.68	0.95	98
1.08 $M_\odot$ … 2.30 $M_\odot$	1.29	2.55	0.77	244
2.30 $M_\odot$ … 51 $M_\odot$	2.19	1.84	0.93	218

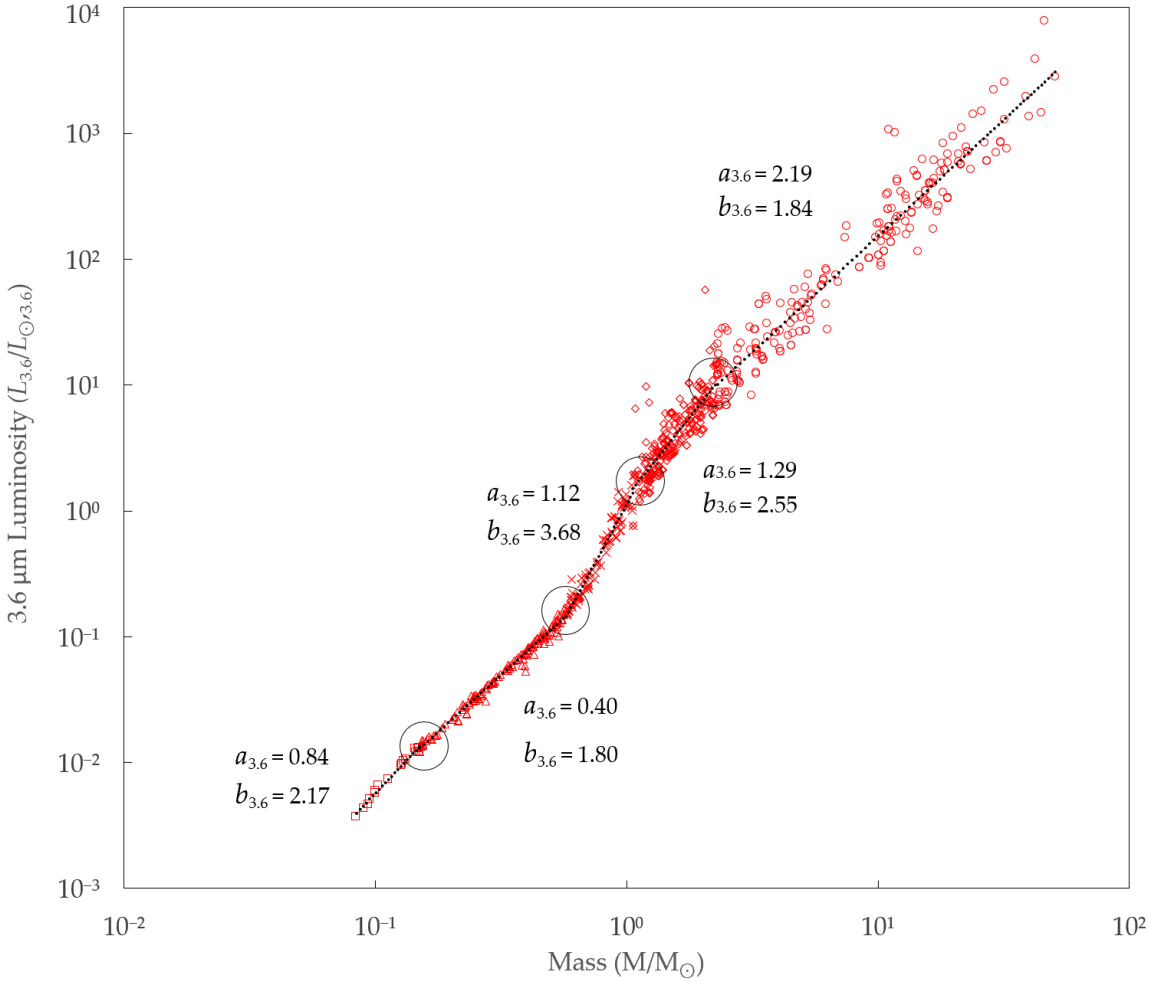

Figure A2. Main Sequence stellar mass–luminosity relation in Spitzer 3.6 μm passband. Based on a sample composed of 4 calibrating data sets: Eker et al. (2015), Malkov (2007), Mann et al. (2015), and Vitrichenko et al. (2007).

Appendix C. Surface Brightness Data Processing

Our sample includes 3.6 μm (Spitzer IRAC channel 1[14]) data from S4G[15] and SPARC[16]. For galaxies where data were available from both sources, we gave priority to S4G.

In total, we used 147 aperture-corrected "1fx2a" profiles from S4G Pipeline 3 (SB_COR) and converted them from magAB/arcsec^2 to $L_{\odot,3.6}$/pc^2 using $10^{-0.4(m_{3.6}-M_{\odot,3.6}-21.572)}$ conversion formula, where $m_{3.6}$ is apparent surface brightness in mag$_{AB}$/arcsec^2, $M_{\odot,3.6}$ is the solar absolute AB

[14] https://irsa.ipac.caltech.edu/data/SPITZER/docs/irac/

[15] https://irsa.ipac.caltech.edu/data/SPITZER/S4G/galaxies/

[16] http://astroweb.cwru.edu/SPARC/

magnitude, adopted at 6.066 mag_{AB} as per baryons.org[17], and the exact value of −21.752 constant equals $5 + 5 \times log_{10}$(1 arcsec).

The following data cleaning procedures were applied. We blank-masked all unresolved S4G datapoints (flagged "INDEF" in source files) and the mid-points of implausible 3-datapoint segments where the central point represents an up-spike > ×4 (or a down-spikes < ×0.25) vs. both surrounding $L_{\odot,3.6}/pc^2$ values. The resulting gaps were then filled with local 2-datapoint exponential fit interpolations. To further reduce peripheral noise, we computed rolling standard deviation starting from the middle of each surface brightness profile to identify the first radial point at with volatility exceeds 0.2, and then applied an outward rolling mean average smoothing from the identified radius, with the smoothing box size set at 10% of the datapoint count.

Cleaned S4G profiles were corrected for inclination using the following procedure. For S4G galaxies with bulges, we subtracted Sérsic bulge models (published in S4G Pipeline 4[18]) from cleaned profiles, and multiplied residual disk $L_{\odot,3.6}/pc^2$ values by a correction factor. Bulges were then added back to inclination-corrected disks. For bulgeless S4G galaxies, the correction factor was applied to unaltered cleaned profiles. Figure A3 illustrates this process.

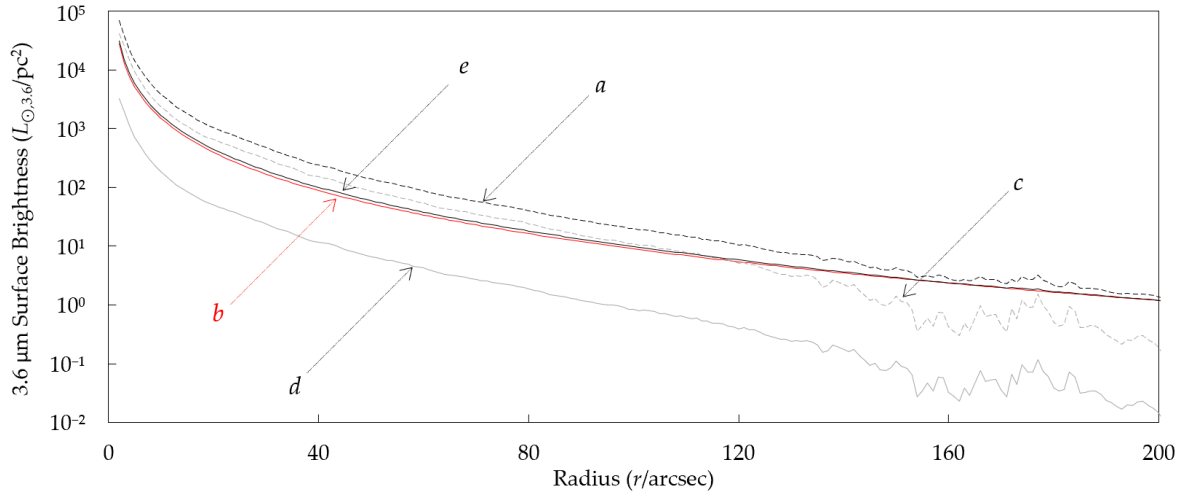

Figure A3. Inclination correction for 90% bulge light-dominated 90° edge-on galaxy NGC7814. (**a**) Clean but uncorrected-for-inclination surface brightness profile from S4G; (**b**) Sérsic bulge with model parameters from S4G P4; (**c**) uncorrected disk profile, the difference between (**a**) and (**b**); (**d**) inclination corrected disk, correction factor 0.078; (**e**) inclination corrected galaxy profile, the sum of the bulge (**b**), and inclination-corrected disk (**d**).

For 103 galaxies from S4G with adopted inclination $i < 70°$, we set the correction factor as $\cos(i)$. For higher-inclined 44 galaxies from S4G ($i \geq 70°$), the correction factor was set as the ratio of true total disk luminosity (based on the outermost aperture-corrected total magnitude TMAG_COR from S4G P3 and bulge models from S4G P4) and of apparent surface brightness integrated over an area of a circle with a radius equal to the semimajor axis of the apparent galactic oval.

We used only 67 profiles from SPARC's database of 175 galaxies[19] for several reasons. SPARC data are based on S4G to an extent, and partially on other sources. The data are of relatively lower resolution than S4G "2a" radial step, and many SPARC profiles include model extrapolations extending out to an equivalent of 32 $mag_{AB}/arccsec^2$ equivalent. In our sample, there were 32 extrapolations by SPARC, in some cases reaching ×2.9 radii of corresponding photometric profiles[20] published by SPARC. We trimmed all such artificial extrapolations. Apart from this, considering that

[17] http://www.baryons.org/ezgal/filters.php

[18] https://www.oulu.fi/astronomy/S4G_PIPELINE4/MAIN/

[19] http://astroweb.cwru.edu/SPARC/MassModels_Lelli2016c.mrt

[20] http://astroweb.cwru.edu/SPARC/sfb_LTG.zip

the surface brightness data from SPARC Table 2 are conveniently smoothed, available in units $L_{\odot,3.6}/pc^2$, and corrected for inclination, we found no further processing necessary. We made sure though that SPARC profiles are indeed inclination-corrected by comparing it with S4G data and with SPARC photometric profiles.

We have not applied light extinction correction. This is not because we agree with the idea that 3.6 μm waveband is virtually lossless. On the contrary, we believe current estimates in the literature might be considerably underestimating light extinction from external galaxies. We simply could not identify any source of reliable information on the matter. Spitzer has a 3.6 μm limiting magnitude of 27 $mag_{AB}/arcsec^2$. This makes the outer ends (>R_{27}) of the surface brightness profiles quite noisy and less reliable for precise modeling. We have not trimmed the profiles at R_{27}, but we would treat conclusions based on post-R_{27} profile tails with caution. In some instances, there is a significant disagreement between S4G and SPARC data. In only 20% of the overlap set, SPARC total magnitude estimates differ from S4G by less than 10%. In the most extreme case (marked as low-quality data), the difference reaches 9 times.

Appendix D. Compilation of Composite RCs

Although only a fraction of galaxies in our sample (58 out of 214) had multiple RC sources, those galaxies are typically the better-researched specimens and we paid particular attention to processing their RC data. Frequently RC sources had pronounced differences not only in velocities, but also in assumed inclinations and distances. The following four-step procedure was applied to resolve conflicts. First, we adopted single inclination and distance, typically the average, but utilizing independent data for a cross-check. Second, we adjusted velocities and positions on the radii of the respective RCs to adopted inclination and distance. Third, we removed single source outlier velocity datapoints, and fourth, averaged individual adjusted RCs to produce a composite RC. Figure A4 provides visualization of this procedure for NGC3521, an example of reasonably good agreement between sources[21], and for NGC2903, a galaxy with pronounced disagreements in RC shapes.

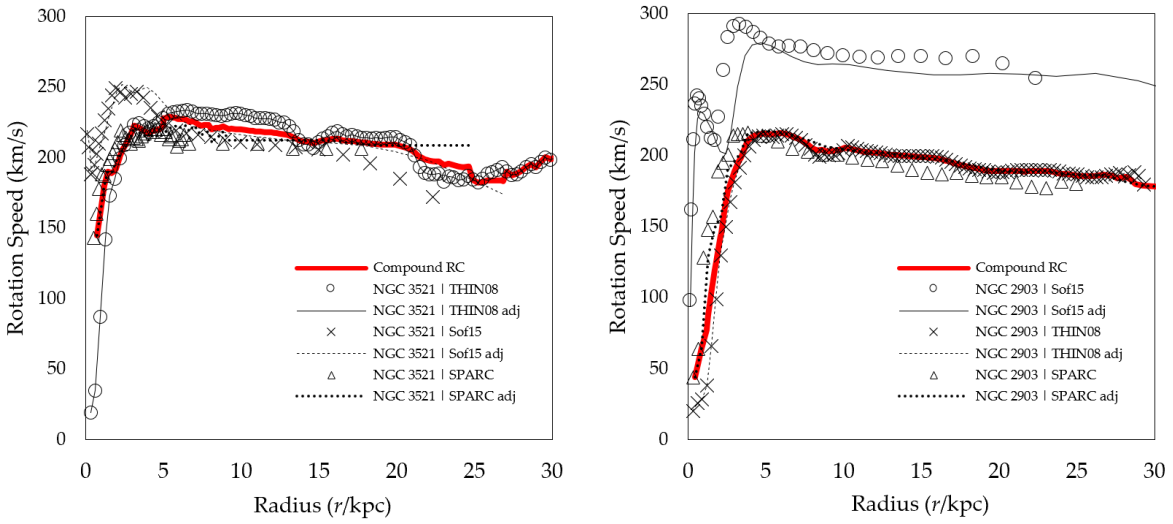

Figure A4. On both charts: *X-axis* shows the distance from the galactic center in kpc; *Y-axis* rotational velocity in km/s; *Circles, triangles, and crosses*—original datapoints from respective sources; *solid and dashed black lines*—RCs adjusted to adopted inclination and distance; and *red curve*—resulting compound RC.

[21] For NGC3521 there is good agreement on velocities, but major differences in distances from 7.7 Mpc (SPARC) to 12 Mpc (NED), and inclinations from 62° (S4G) to 75° (Sofue, SPARC).

Appendix E. Summary Metadata for 214 Galaxies

Galaxy ID (A to Z)	Hubble Type	Adopted Inclination	Adopted Distance	RC Max Velocity	S4G Total Luminosity	SPARC Total Luminosity	R_{27} Estimate	Light Source	RC Source(s)
		Degrees	Mpc	km/s	$10^9\ L_{\odot,3.6}$	$10^9\ L_{\odot,3.6}$	kpc	1 = S4G 2 = SPARC	Compilation by * SPARC, ** Sofue
CamB	10	65	3.35	20.10	n/a	0.07	1.63	2	8 *
D512-2	10	56	15.20	37.20	n/a	0.25	5.60	2	64 *
D564-8	10	63	8.78	25.00	n/a	0.03	1.45	2	64 *
D631-7	10	59	6.94	58.50	n/a	0.19	2.49	2	64 *, 26 *
DDO064	10	60	6.97	46.90	0.11	0.15	4.10	1	23 *, 62 *
DDO154	10	60.2	4.00	48.72	0.03	0.05	1.71	1	5 *, 13 *, 22
DDO161	10	70	7.35	67.50	0.44	0.53	6.63	1	20 *
DDO168	10	63	4.32	55.00	0.16	0.18	3.93	1	57 *, 12 *
DDO170	10	66	18.94	62.20	n/a	0.49	9.00	2	5 *, 41 *
ESO079-G014	4	79	30.14	178.00	48.86	45.34	23.96	1	33 *
ESO116-G012	7	74	16.82	112.00	7.67	4.39	14.52	1	33 *
ESO444-G084	10	32	5.21	63.10	n/a	0.08	1.77	2	20 *
ESO563-G021	4	83	69.58	321.00	n/a	311.81	51.28	2	61 *
F561-1	9	24	66.40	50.40	n/a	3.58	11.59	2	24 *, 25 *
F563-1	9	25	48.90	112.50	n/a	1.94	11.38	2	40 *, 25 *
F563-V1	10	60	54.00	29.50	n/a	0.94	12.04	2	24 *, 25 *
F563-V2	10	29	59.70	118.00	n/a	2.99	11.58	2	26 *, 25 *
F565-V2	10	60	51.80	83.10	n/a	0.54	7.03	2	24 *, 25 *
F567-2	9	20	79.00	52.20	n/a	1.76	10.72	2	24 *, 25 *
F568-1	5	26	90.70	142.00	n/a	5.60	16.71	2	26 *, 25 *
F568-3	7	40	82.40	120.00	n/a	7.67	21.57	2	40 *, 25 *
F568-V1	7	40	80.60	118.00	n/a	3.90	11.72	2	26 *, 25 *
F571-8	5	85	53.30	144.00	n/a	10.67	12.92	2	26 *, 25 *
F571-V1	7	30	80.10	84.30	n/a	1.77	10.10	2	24 *, 25 *
F574-1	7	65	96.80	99.70	n/a	5.67	16.89	2	26 *, 25 *
F574-2	9	30	89.10	40.00	n/a	2.42	12.96	2	24 *, 25 *
F579-V1	5	26	89.50	114.00	n/a	11.34	16.49	2	26 *, 25 *
F583-1	9	63	35.40	86.90	n/a	1.00	8.24	2	40 *, 25 *
F583-4	5	55	53.30	69.90	n/a	1.74	7.75	2	40 *, 25 *
IC2574	9	75	3.91	65.21	1.68	0.99	10.62	1	57 *, 45 *, 22
IC4202	4	90	108.32	250.00	n/a	170.92	55.67	2	61 *
KK98-251	10	59	6.80	34.60	n/a	0.08	4.21	2	7 *
NGC0024	5	64	7.38	110.00	3.54	4.86	8.16	1	27 *, 18 *
NGC0100	6	89	15.37	91.20	3.82	3.12	12.37	1	23 *, 51 *
NGC0157	4	45	21.47	196.90	111.52	n/a	19.15	1	54 **
NGC0247	7	74	3.66	108.00	7.69	6.57	16.86	1	57 *, 14 *
NGC0253	5	79.8	3.17	212.72	85.08	n/a	33.83	1	38
NGC0289	4	46	20.96	194.00	70.03	62.58	24.19	1	70 *
NGC0300	7	42	1.96	96.12	4.28	2.78	7.49	1	57 *, 15 *, 39 **
NGC0660	1	70	13.93	188.24	74.04	n/a	20.66	1	60
NGC0801	5	80	70.33	238.00	n/a	348.70	49.10	2	57 *, 12 *
NGC1003	6	67	11.40	115.00	n/a	6.35	10.50	2	57 *, 12 *, 60
NGC1090	4	64	34.23	176.00	62.52	73.94	30.87	1	33 *
NGC1097	3	40	17.00	358.58	245.23	n/a	35.43	1	60
NGC1365	3	46	17.53	274.77	261.47	n/a	46.91	1	59
NGC1705	11	80	5.60	73.20	0.48	0.59	2.33	1	43 *
NGC1808	1	58	11.04	207.00	80.08	n/a	17.98	1	59
NGC2366	10	68	3.27	53.70	n/a	0.23	2.73	2	43 *
NGC2403	6	63	3.20	137.19	n/a	10.03	9.37	2	21 *, 30 *, 22, 59
NGC2683	3	80	9.52	212.00	65.34	68.53	18.56	1	57 *, 12 *
NGC2841	3	73.7	14.10	325.22	167.02	131.07	26.66	1	27 *, 5 *, 22, 59
NGC2903	4	65.2	8.74	215.75	85.55	78.84	18.82	1	5 *, 4 *, 22, 59
NGC2915	11	56	4.13	86.50	n/a	0.57	2.93	2	28 *
NGC2955	3	56	97.53	276.00	n/a	298.94	62.42	2	61 *
NGC2976	5	61	3.58	88.99	3.58	2.42	4.72	1	58 *, 22
NGC2998	5	58	64.25	214.00	n/a	165.97	35.51	2	57 *, 12 *
NGC3031	2	59	3.60	251.23	96.26	n/a	17.63	1	60, 22, 59
NGC3041	5	35.9	23.14	130.12	39.01	n/a	17.50	1	44 **

NGC3109	9	70	1.32	67.30	n/a	0.19	6.40	2	5 *, 36 *
NGC3198	5	71.5	13.80	161.81	35.51	38.04	21.14	1	21 *, 5 *, 4 *, 22, 59
NGC3521	4	72.7	10.70	229.95	153.77	80.52	24.69	1	21 *, 57 *, 22, 59
NGC3628	3	87	9.93	227.24	97.09	n/a	29.82	1	59
NGC3672	5	67	26.63	218.99	97.67	n/a	19.62	1	60
NGC3726	5	53	16.06	169.00	51.95	63.67	19.00	1	69 *, 56 *
NGC3741	10	70	3.23	51.60	n/a	0.02	0.91	2	34 *, 6 *
NGC3769	3	70	16.34	126.00	14.20	15.36	11.09	1	69 *, 56 *
NGC3893	5	49	18.04	194.00	60.80	51.76	13.82	1	69 *, 56 *
NGC3917	6	79	17.59	138.00	18.46	21.45	16.89	1	69 *, 56 *
NGC3949	4	55	17.51	169.00	32.62	27.51	10.19	1	69 *, 56 *
NGC3953	4	62	17.18	224.00	111.05	111.46	19.99	1	69 *, 56 *
NGC3972	4	77	18.55	134.00	13.56	12.96	14.39	1	69 *, 56 *
NGC3976	3	60	35.82	210.76	112.00	n/a	32.30	1	44 **
NGC3992	4	56	23.07	272.00	199.35	171.03	35.35	1	69 *, 56 *
NGC4010	7	89	18.02	129.00	15.19	15.52	16.25	1	69 *, 56 *
NGC4013	3	89	17.94	198.00	78.06	44.36	21.22	1	69 *, 56 *
NGC4051	4	49	14.99	161.00	59.16	62.07	16.86	1	69 *, 56 *
NGC4068	10	44	4.45	41.90	0.19	0.22	2.35	1	43 *
NGC4085	5	82	18.29	136.00	20.81	20.24	8.51	1	69 *, 56 *
NGC4088	4	69	15.82	182.00	75.20	102.76	18.56	1	69 *, 56 *
NGC4100	4	73	19.59	195.00	63.30	52.13	19.76	1	69 *, 56 *
NGC4138	0	53	17.31	195.00	37.36	27.15	12.25	1	69 *, 56 *
NGC4157	3	82	17.50	201.00	94.30	100.43	23.76	1	69 *, 56 *
NGC4183	6	82	17.43	115.00	8.69	10.71	16.06	1	69 *, 56 *
NGC4192	2	74	14.80	236.98	91.18	n/a	26.68	1	59
NGC4217	3	86	18.62	191.00	88.63	83.35	29.06	1	69 *, 56 *
NGC4244	6	84.5	4.10	99.06	3.54	n/a	12.99	1	49 **
NGC4258	4	67	7.62	232.71	91.71	n/a	39.79	1	59
NGC4303	4	25	16.50	152.31	137.66	n/a	22.08	1	59
NGC4321	4	27	17.09	270.88	183.52	n/a	30.83	1	59
NGC4395	9	46	4.51	83.80	1.60	2.35	7.66	1	63 *, 62 *, 44 **
NGC4536	4	67	17.07	184.99	81.96	n/a	25.99	1	59
NGC4559	6	67	9.32	124.00	19.48	19.09	17.53	1	1 *
NGC4565	3	86	12.65	260.35	161.22	n/a	37.54	1	59
NGC4631	7	84	6.57	183.59	36.67	n/a	27.86	1	59
NGC4736	2	41.4	4.70	198.29	51.46	n/a	16.09	1	60, 22, 59
NGC4826	2	65.2	6.28	190.10	66.18	n/a	12.78	1	22 **
NGC5005	4	68	18.91	265.00	212.56	163.55	22.55	1	52 *
NGC5033	5	66	15.70	225.00	107.85	112.15	30.75	1	57 *, 4 *, 60, 59
NGC5055	4	56.2	9.90	210.75	155.71	147.54	31.39	1	2 *, 10 *, 60, 22, 59
NGC0891	3	90	9.91	234.00	n/a	127.04	20.71	2	31 *
NGC5236	5	24	6.78	239.46	197.90	n/a	21.49	1	60
NGC5371	4	53	35.04	242.00	241.30	324.43	26.16	1	57 *, 4 *
NGC5585	7	51	7.86	92.30	3.41	2.95	7.93	1	9 *, 57 *, 19 *
NGC5678	3	46.4	32.21	183.11	134.63	n/a	23.11	1	44 **
NGC5907	5	88	16.37	248.97	143.49	156.90	40.48	1	57 *, 55 *, 60, 59
NGC5985	3	60	43.53	305.00	240.41	189.55	38.83	1	10 *, 12 *
NGC6015	6	60	16.86	166.00	31.01	32.16	18.47	1	67 *
NGC6195	3	62	137.08	258.00	n/a	346.31	70.45	2	61 *
NGC6503	6	74	6.07	121.00	11.12	12.46	9.35	1	5 *, 4 *
NGC6674	3	54	51.20	291.00	n/a	209.11	39.72	2	57 *, 12 *, 60
NGC6946	6	38	5.62	181.92	n/a	64.56	16.89	2	11 *, 60 *, 22, 59
NGC7331	3	75	14.25	258.03	n/a	200.29	31.13	2	5 *, 4 *, 60, 22, 59
NGC7793	7	49.6	3.85	114.66	7.62	6.99	7.42	1	27 *, 57 *, 15 *, 22
NGC7814	2	90	15.39	250.00	81.52	66.86	28.05	1	31 *
PGC51017	11	66	13.49	20.50	n/a	0.16	2.22	2	43 *
UGC00128	8	57	66.37	134.00	n/a	12.08	23.81	2	68 *, 65 *
UGC00191	9	45	16.74	83.85	1.46	2.12	6.33	1	40 *, 66 *
UGC00634	9	37	29.19	108.00	2.20	1.96	10.75	1	66 *
UGC00731	10	57	11.80	73.90	n/a	0.32	7.55	2	63 *, 62 *
UGC00763	9	42	13.95	105.11	9.46	n/a	9.47	1	29
UGC00891	9	60	9.78	63.75	0.26	0.33	3.98	1	66 *
UGC01230	9	22	55.33	113.00	n/a	8.26	16.63	2	23 *, 65 *

UGC01281	8	90	5.27	56.90	n/a	0.31	7.15	2	23 *, 62 *, 63 **
UGC02023	10	19	10.10	58.80	n/a	0.91	6.66	2	63 *, 62 *, 63 **
UGC02259	8	41	10.27	90.00	n/a	1.62	7.87	2	5 *, 16 *
UGC02455	10	51	7.34	61.00	n/a	3.18	7.35	2	63 *, 62 *, 63 **
UGC02487	0	36	71.36	383.00	n/a	331.77	51.89	2	48 *, 47 *
UGC02885	5	64	83.11	305.00	n/a	394.69	63.66	2	57 *, 53 *
UGC02916	2	50	65.40	217.71	n/a	123.32	31.07	2	48 *, 47 *, 48 **
UGC02953	2	50	16.50	319.00	n/a	259.77	26.72	2	48 *, 47 *, 48 **
UGC03205	2	67	49.84	237.00	n/a	116.35	23.20	2	48 *, 47 *, 48 **
UGC03546	1	55	28.70	257.89	n/a	80.74	19.48	2	48 *, 47 *, 48 **
UGC03580	1	63	20.70	129.77	n/a	13.41	12.04	2	48 *, 47 *, 48 **
UGC04273	3	61	34.07	209.69	51.36	n/a	18.83	1	29
UGC04278	7	90	11.77	92.80	1.71	1.29	10.15	1	23 *, 62 *
UGC04284	5	59	11.04	122.26	4.15	n/a	8.88	1	29
UGC04305	10	40	3.40	36.60	0.45	0.76	4.91	1	63 *, 62 *, 63 **
UGC04325	9	41	10.31	92.70	1.98	1.96	6.50	1	63 *, 62 *
UGC04483	10	58	3.43	24.30	0.02	0.01	0.93	1	43 *, 42 *
UGC04499	8	50	11.98	74.30	1.00	1.42	5.69	1	63 *, 62 *
UGC04543	7	40	30.29	67.92	3.77	n/a	14.10	1	29
UGC04605	2	74	25.45	227.22	58.60	n/a	18.75	1	48 **
UGC04936	5	35	27.22	257.85	36.90	n/a	24.81	1	29
UGC05005	10	41	55.33	100.00	n/a	4.53	11.27	2	23 *, 65 *
UGC05253	2	37	21.50	248.00	127.83	171.32	31.48	1	48 *, 47 *, 48 **
UGC05316	5	68	18.24	143.03	7.93	n/a	17.16	1	29
UGC05414	10	55	11.19	61.40	1.43	0.88	7.38	1	63 *, 62 *
UGC05716	9	54	20.71	74.70	n/a	0.54	4.42	2	66 *
UGC05721	7	61	6.18	80.87	0.49	0.55	2.64	1	23 *, 62 *, 63 **
UGC05750	8	64	60.21	78.90	n/a	3.37	15.76	2	26 *, 65 *
UGC05764	10	60	8.42	55.80	0.06	0.08	2.69	1	66 *
UGC05789	5	61	14.33	123.77	9.68	n/a	14.32	1	29
UGC05829	10	34	8.64	68.60	0.55	0.51	5.45	1	63 *, 62 *, 63 **
UGC05918	10	46	7.66	44.50	0.07	0.22	6.06	1	63 *, 62 *, 63 **
UGC05931	5	56	24.29	143.28	20.83	n/a	11.40	1	29
UGC05982	5	56	25.68	193.98	49.56	n/a	15.44	1	29
UGC05986	9	90	8.70	116.05	4.80	4.61	15.27	1	63 *, 62 *, 63 **
UGC05999	10	22	48.79	100.00	n/a	2.95	10.88	2	24 *, 65 *
UGC06399	9	75	18.41	87.60	2.03	2.19	9.82	1	69 *, 56 *
UGC06446	7	51	12.00	83.20	0.91	0.95	4.92	1	69 *, 56 *, 63 **
UGC06614	1	36	91.38	205.00	n/a	102.19	29.78	2	26 *, 65 *
UGC06628	9	20	15.30	42.45	2.85	2.95	8.16	1	63 *, 62 *, 63 **
UGC06786	0	64	28.97	231.47	63.33	78.05	20.23	1	48 *, 47 *, 48 **
UGC06787	2	66	21.30	276.00	82.59	98.19	22.10	1	48 *, 47 *, 48 **
UGC06818	9	75	18.13	74.40	1.39	1.49	7.38	1	69 *, 56 *
UGC06903	6	32.4	30.01	159.06	15.17	n/a	12.80	1	46 **
UGC06917	9	56	18.51	111.00	5.43	5.90	12.02	1	69 *, 56 *
UGC06918	3	30	21.75	158.40	36.13	n/a	8.86	1	46 **
UGC06923	10	65	17.90	81.10	n/a	2.38	7.70	2	69 *, 56 *
UGC06930	7	32	17.13	109.00	8.00	8.28	10.63	1	69 *, 56 *
UGC06973	2	71	21.20	180.00	72.57	37.80	12.13	1	69 *, 56 *
UGC06983	6	49	19.53	113.00	5.02	4.57	11.55	1	69 *, 56 *
UGC07089	8	80	14.63	79.10	2.18	3.36	10.22	1	69 *, 56 *
UGC07125	9	90	19.50	65.46	2.27	2.68	12.48	1	63 *, 62 *, 63 **
UGC07151	6	90	6.63	76.20	2.03	2.10	9.90	1	63 *, 62 *, 63 **
UGC07232	10	59	2.89	44.00	0.09	0.09	1.23	1	63 *, 62 *
UGC07261	8	30	9.10	76.10	1.57	1.64	6.09	1	63 *, 62 *, 63 **
UGC07278	10	15	3.30	80.60	2.30	1.16	4.54	1	43 *, 63 *
UGC07323	8	47	8.00	85.60	3.48	3.68	7.29	1	63 *, 62 *, 63 **
UGC07399	8	55	8.43	104.81	1.02	1.08	3.84	1	63 *, 62 *, 63 **
UGC07559	10	61	4.25	32.77	0.07	0.11	2.14	1	63 *, 62 *, 63 **
UGC07577	10	63	2.92	17.80	0.13	0.04	2.92	1	63 *, 62 *, 63 **
UGC07603	7	78	6.80	64.00	0.65	0.37	5.00	1	63 *, 62 *, 63 **
UGC07608	10	25	8.26	69.30	0.20	0.23	3.86	1	63 *, 62 *, 63 **
UGC07690	10	41	8.11	60.70	0.65	0.77	3.22	1	63 *, 62 *, 63 **
UGC07866	10	44	5.03	33.10	0.11	0.11	2.63	1	63 *, 62 *

UGC08286	6	90	6.50	84.30	1.10	1.24	7.00	1	63 *, 62 *, 63 **
UGC08490	9	50	4.90	80.18	1.00	0.98	4.09	1	63 *, 62 *, 63 **
UGC08550	7	90	6.70	57.50	0.34	0.28	4.03	1	63 *, 62 *, 63 **
UGC08699	2	73	39.30	202.86	46.19	50.98	16.77	1	48 *, 47 *, 48 **
UGC08837	10	80	6.17	48.00	0.30	0.47	5.45	1	63 *, 62 *, 63 **
UGC09037	6	65	82.15	160.00	n/a	56.24	39.03	2	35 *
UGC09133	2	53	57.10	289.00	n/a	281.14	40.42	2	48 *, 47 *, 48 **
UGC09649	3	65	9.47	94.81	2.61	n/a	6.61	1	29
UGC09753	4	69	14.82	137.64	18.78	n/a	12.50	1	29
UGC09837	5	31.3	42.41	157.70	15.66	n/a	14.80	1	46 **
UGC09858	4	79	38.88	160.87	43.02	n/a	31.29	1	29
UGC09992	10	30	10.57	34.30	0.24	0.32	4.10	1	63 *, 62 *
UGC10310	9	34	15.20	72.95	1.15	1.66	6.78	1	63 *, 62 *, 63 **
UGC10359	6	32	17.47	138.20	12.11	n/a	11.35	1	29
UGC10445	6	45	21.25	78.64	4.41	n/a	9.07	1	29
UGC10470	4	43	24.17	165.51	58.12	n/a	13.83	1	29
UGC10546	6	54	22.63	107.80	7.17	n/a	10.97	1	29
UGC10897	5	30	22.53	119.73	24.66	n/a	10.27	1	29
UGC11455	6	90	81.46	291.00	n/a	373.93	40.28	2	61 *
UGC11557	8	30	23.70	84.50	n/a	12.21	10.34	2	62 *, 26 *, 63 **, 32 **
UGC11820	9	45	17.67	84.45	n/a	1.51	6.17	2	40 *, 66 *
UGC12343	5	42	31.41	225.26	186.25	n/a	26.19	1	29
UGC12506	6	86	99.47	255.00	n/a	136.10	67.69	2	35 *
UGC12632	9	46	9.44	74.86	n/a	1.26	8.42	2	63 *, 62 *, 32 **, 63 **
UGC12732	9	39	13.20	98.00	1.29	1.64	7.55	1	63 *, 62 *
UGC12754	5	49	12.10	125.80	9.48	n/a	8.57	1	29
UGCA442	9	64	4.76	57.80	0.14	0.14	3.55	1	20 *
UGCA444	10	78	1.00	38.30	0.11	0.01	3.39	1	37 *

Appendix F. Rotation Curves Data Sources

Code	External Reference (A to Z)		
1	Barbieri, C.V. et al. 2005, A&A 439, 947	36	Jobin, M. & Carignan, C. 1990, AJ, 100, 648
2	Battaglia, G. et al. 2006 A&A 447 49	37	Kepley, A.A. et al. 2007, AJ, 133, 2242
3	Battaglia, G. et al. 2006, A&A, 447, 49	38	k-Larrondo, J. et al. 2011 MNRAS, 411, 71
4	Begeman, K.G. 1987, PhD thesis, Univers. of Groningen	39	k-Larrondo, J. et al. 2011 MNRAS, 416, 509
5	Begeman, K.G. et al. 1991, MNRAS, 249, 523	40	Kuzio de Naray, R. et al. 2008, ApJ, 676, 920
6	Begum, A. et al. 2005, A&A 433, L1	41	Lake, G. et al. 1990, AJ, 99, 547
7	Begum, A. & Chengalur, J.N. 2004, A&A, 424, 509	42	Lelli, F. et al. 2012, A&A, 544, A145
8	Begum, A. et al. 2003, New A, 8, 267	43	Lelli, F. et al. 2014, A&A, 566, A71
9	Blais-Ouellette, S. et al. 1999, AJ, 118, 2123	44	Marquez I. et al. 2002 A&A, 393, 389
10	Blais-Ouellette, S. et al. 2004, A&A, 420, 147	45	Martimbeau, N. & Carignan, C. 1994, AJ, 107, 543
11	Boomsma, R. et al. 2008, A&A, 490, 555	46	Martinsson et al. 2013 A&A 557
12	Broeils, A.H. 1992, PhD thesis, University of Groningen	47	Noordermeer, E. et al. 2005, A&A, 442, 137
13	Carignan, C. & Beaulieu, S. 1989, AJ, 347, 192	48	Noordermeer, E. et al. 2007, MNRAS, 376, 1513
14	Carignan, C. & Puche, D. 1990a, AJ, 100, 394	49	Olling, R.P. 1996 AJ, 122, 457
15	Carignan, C. & Puche, D. 1990b, AJ, 100, 641	50	Puche, D. et al. 1991, AJ, 101, 447
16	Carignan, C. et al. 1988, AJ, 95, 37	51	Rhee, M. & vanAlbada, T.S. 1996, A&AS, 115, 407
17	Casertano, S. & van Gorkom, J.H. 1991, ApJ, 101, 1231	52	Richards, E.E. et al. 2015, MNRAS, 449, 3981
18	Chemin, L. et al. 2006, AJ, 132, 2527	53	Roelfsema, P.R. & Allen, R.J. 1985, A&A, 146, 213
19	Cote, S. et al. 1991, AJ, 102, 904	54	Ryder S.D. et al. 1998 MNRAS 293, 411
20	Cote, S. et al. 2000, AJ, 120, 3027	55	Sancisi & vanAlbada. 1987, in IAU Symp. 117, 67
21	Daigle, O. et al. 2006, MNRAS, 367, 469	56	Sanders. & Verheijen. 1998, ApJ, 503, 97
22	de Blok W.J.G. et al. 2008 AJ 136 2648	57	Sanders, R.H. 1996, ApJ, 437, 117
23	de Blok, W.J.G. & Bosma, A. 2002, A&A, 385, 816	58	Simon, J.D. et al. 2003, 596, 957
24	de Blok, W.J.G. & McGaugh, S.S. 1997, MNRAS, 290, 533	59	Sofue, Y. 2015 PASJ, 68, 2
25	de Blok, W.J.G. et al. 1996, MNRAS, 283, 18	60	Sofue, Y. et al. 1999 AJ, 523, 136
26	de Blok, W.J.G. et al. 2001, AJ, 122, 2396	61	Spekkens, K. & Giovanelli, R. 2006, AJ, 132, 1426
27	Dicaire, I. et al. 2008, MNRAS, 385, 553	62	Swaters, R.A. 2002, A&A, 390, 829
28	Elson, E.C. et al. 2010, MNRAS, 404, 2061	63	Swaters, R.A. 2009, A&A, 493, 871
29	Epinat B. et al., 2008 MNRAS, 388, 500	64	Trachternarch, C. et al. 2009, A&A, 505, 577
30	Fraternali F. et al. 2002 AJ 123 3124	65	van der Hulst, J.M. et al. 1993, AJ, 106, 548
31	Fraternali, F. et al. 2011, A&A, 531, A64	66	van Zee, L. 1997, AJ, 113, 1618
32	Garrido et al. 2005 MNRAS, 362, 127	67	Verdes-Montenegro, L. et al. 1997, A&A, 321, 754

33	Gentile, G. et al. 2004, MNRAS, 351, 903	68	Verheijen & de Blok, 1999, Ap&SS, 269, 673
34	Gentile, G. et al. 2007, MNRAS, 375, 199	69	Verheijen & Sancisi, 2001, A&A, 370, 765
35	Hallenbeck, G. et al. 2014, AJ, 148, 69	70	Walsh, W. et al. 1997, AJ, 113, 1591.

References

1. De Blok, W.J.G. The core-cusp problem. *Adv Astron*. **2010**, Available online: https://www.hindawi.com/journals/aa/2010/789293/ (accessed on 24 April 2020).
2. Ogiya, G.; Mori, M. The core-cusp problem in cold dark matter halos and supernova feedback: effects of oscillation. *Astrophys. J*. **2014**, *793*, 46.
3. Genina, A.; Benítez-Llambay, A.; Frenk, C.S., Cole S., Fattahi A., Navarro J.F., Oman K.A., Sawala T., Theuns T. The core–cusp problem: a matter of perspective. *Mon. Not. R. Astron. Soc*. **2018**, *474*, 1398–1411.
4. Undagoitia, T.M.; Rauch, L. Dark matter direct-detection experiments. *J. Phys. G Nucl. Part Phys.* **2015**, *43*, 013001.
5. Smith, P.F.; Smith, N.J.T.; Lewin, J.D.; Homer G.J.; Alner G. J.; Arnison G.T.J.; Quenby J.J.; Sumner T.J.; Bewick A.; Ali T.; et al. Dark matter experiments at the UK Boulby Mine UK Dark Matter Collaboration. *Phys. Rep.* **1998**, *307*, 275–282.
6. Lewin, J.D.; Smith, P.F. *Review of Mathematics, Numerical Factors, and Corrections for Dark Matter Experiments Based on Elastic Nuclear Recoil*. SCAN-9603159; *Astropart. Phys.* **1996**, *6*, 87–112.
7. Billard, J.; Figueroa-Feliciano, E.; Strigari, L. Implication of neutrino backgrounds on the reach of next generation dark matter direct detection experiments. *Phys. Rev. D*. **2014**, *89*, 023524.
8. Chang, J.; Ambrosi, G.; An, Q.; Asfandiyarov R.; Azzarello P.; Bernardini P.; Bertucci B.; Cai M.S.; Caragiulo M., Chen D.Y.; et al. The DArk matter particle explorer mission. *Astropart. Phys.* **2017**, *95*, 6–24.
9. Bertone, G.; Hooper, D.; Silk, J. Particle dark matter: Evidence, candidates and constraints. *Phys. Rep.* **2005**, *405*, 279–390.
10. Berezinsky, V.; Valle, J.W. The KeV majoron as a dark matter particle. *Phys. Lett B* **1993**, *318*, 360–366.
11. Sofue, Y.; Rubin, V. Rotation curves of spiral galaxies. *Annu. Rev. Astron. Astrophys.* **2001**, *39*, 137–174.
12. Rubin, V.C.; Ford Jr, W.K.; Thonnard, N. Rotational properties of 21 SC galaxies with a large range of luminosities and radii, from NGC 4605/R= 4kpc/to UGC 2885/R= 122 kpc. *Astrophys. J.* **1980**, *238*, 471–487.
13. Rubin, V.C. The rotation of spiral galaxies. *Science* **1983**, *220*, 1339–1344.
14. Rubin, V.C.; Ford Jr, W.K.; Thonnard, N. Extended rotation curves of high-luminosity spiral galaxies. IV-Systematic dynamical properties, SA through, S.C. *Astrophys. J.* **1978**, *225*, L107–L111.
15. Adams, F.C.; Walker, T.P. Brown dwarfs as dark galactic halos. *Astrophys. J.* **1990**, *359*, 57–62.
16. Ivanov, P.; Naselsky, P.; Novikov, I. Inflation and primordial black holes as dark matter. *Phys. Rev. D*. **1994**, *50*, 7173.
17. Carr, B; Kühnel, F.; Sandstad, M. Primordial black holes as dark matter. *Phys. Rev. D*. **2016**, *94*, 083504.
18. Pfenniger, D.; Combes, F. Is dark matter in spiral galaxies cold gas? I.I. Fractal models and star non-formation. *Astron. Astrophys.* **1994**, *285*, 94–118.
19. Heithausen, A. Molecular hydrogen as baryonic dark matter. *Astrophys. J. Lett*. **2004**, *606*, L13.
20. Milgrom, M. A modification of the Newtonian dynamics as a possible alternative to the hidden mass hypothesis. *Astrophys. J.* **1983**, *270*, 365–370.
21. Sanders, R.H.; McGaugh, S.S. Modified Newtonian dynamics as an alternative to dark matter. *Annu. Rev. Astron. Astrophys.* **2002**, *40*, 263–317.
22. Kroupa, P. The dark matter crisis: problems with the current standard model of cosmology and steps towards an improved model. In Proceedings of the Probes of Dark Matter on Galaxy Scales, AAS Topical Conference Series Vol. 1, Monterey, CA, USA, 14–19 July 2013.
23. Van Dokkum, P.; Danieli, S.; Cohen, Y.; Merritt A.; Romanowsky A.J.; Abraham R.; Brodie J.; Charlie C.; Lokhorst D.; Mowla L.; et al. A galaxy lacking dark matter. *Nature* **2018**, *555*, 629–632.
24. Feng, J.Q.; Gallo, C.F. Mass distribution in rotating thin-disk galaxies according to Newtonian dynamics. *Galaxies* **2014**, *2*, 199–222.
25. Rubin, V.C. Dark matter in the universe. *Proc. Am. Philos. Soc*. **1988**, *132*, 434–443.
26. Rubin, V.C. Galaxy dynamics and the mass density of the universe. *Proc. Natl. Acad. Sci. USA* **1993**, *90*, 4814–4821.

27. Komatsu, E.; Smith, K.; Dunkley, J.; Bennett C.L.; Gold B.; Hinshaw G.; Jarosik N.; Larson D.; Nolta M.R.; Page L.; et al. Seven-year wilkinson microwave anisotropy probe (WMAP*) observations: cosmological interpretation. *Astrophys. J. Suppl. Ser*. **2011**, *192*, 18.
28. Hinshaw, G.; Larson, D.; Komatsu, E.; Spergel D.N.; Bennett C.L.; Dunkley J., Nolta M.R., Halpern M., Hill R.S.; Odegard N.; et al. Nine-year Wilkinson Microwave Anisotropy Probe (WMAP) observations: cosmological parameter results. *Astrophys. J. Suppl. Ser*. **2013**, *208*, 19.
29. Pavlovich, K.; Pavlovich, A.; Sipols, A. Newtonian explanation of galaxy rotation curves based on distribution of baryonic matter. *In ArXiv Prepr ArXiv14062401;* **2014**. Available online: https://arxiv.org/abs/1406.2401 (accessed on 24 April 2020).
30. Jałocha, J.; Bratek, L.; Kutschera, M.; Skindzier, P. Global disc models for galaxies NGC 1365, 6946, 7793 and UGC 6446. *Mon. Not. R. Astron. Soc*. **2010**, *406*, 2805–2816.
31. Chemin, L.; Carignan, C.; Foster, T. HI kinematics and dynamics of Messier 31. *Astrophys. J.* **2009**, *705*, 1395.
32. Geehan, J.J.; Fardal, M.A.; Babul, A.; Guhathakurta, P. Investigating the Andromeda stream—I. Simple analytic bulge—disc—halo model for M31. *Mon. Not. R. Astron. Soc*. **2006**, *366*, 996–1011.
33. Golse, G.; Kneib J-P. Pseudo elliptical lensing mass model: Application to the NFW mass distribution. *Astron. Astrophys.* **2002**, *390*, 821–827.
34. Sofue, Y. Dark Halos of M31 and the Milky Way. *Publ. Astron. Soc. Jpn*. **2015**, *67*, 75. doi:10.1093/pasj/psv042
35. Lelli, F.; McGaugh, S.S.; Schombert, J.M. SPARC: mass models for 175 disk galaxies with Spitzer photometry and accurate rotation curves. *Astron. J.* **2016**, *152*, 157.
36. Walter, F.; Brinks, E.; De Blok, W.; Bigiel F.; Kennicutt Jr. R.C.; Thornley M.D.; Leroy A.K.;. THINGS: The HI nearby galaxy survey. *Astron. J.* **2008**, *136*, 2563.
37. Querejeta, M.; Meidt, S.E.; Schinnerer, E.; Cisternas M.; Muñoz-Mateos J.C.; Sheth K.; Knapen J.; Van de Ven G.; Norris M.; Peletier R.; et al. The Spitzer Survey of Stellar Structure in Galaxies (S4G): precise stellar mass distributions from automated dust correction at 3.6 μm. *Astrophys. J. Suppl. Ser*. **2015**, *219*, 5.
38. Salo, H.; Laurikainen, E.; Laine, J.; Comerón S.; Gadotti D.; Buta R.; Sheth K.; Zaritsky D.; Ho L.; Knapen J.; et al. The Spitzer Survey of Stellar Structure in Galaxies (S4G): Multi-component decomposition strategies and data release. *Astrophys. J. Suppl. Ser*. **2015**, *219*, 4.
39. Muñoz-Mateos, J.C.; Sheth, K.; Regan, M.; Kim T.; Laine J.; Erroz- Ferrer S.; Gil de Paz A.; Comeron S.; Hinz J.; Laurikainen E.; et al. The Spitzer Survey of stellar structure in galaxies (S4G): stellar masses, sizes, and radial profiles for 2352 nearby galaxies. *Astrophys. J. Suppl. Ser*. **2015**, *219*, 3.
40. Buta, R.J.; Sheth, K.; Athanassoula, E.; Bosma A.; Knapen J.H.; Laurikainen E.; Salo H.; Elmegreen D.; Ho L.C.; Zaritsky D.; et al. A classical morphological analysis of galaxies in the Spitzer survey of stellar structure in galaxies (S4G). *Astrophys. J. Suppl. Ser*. **2015**, *217*, 32.
41. Walter, F.; Brinks, E.; de Blok, W.; Thornley, M.D.; Kennicutt, R. First Results from THINGS: The HI Nearby Galaxy Survey. Extra-planar GAS ASP Conference Series, Vol.331, **2005**. Available online: https://arxiv.org/abs/astro-ph/0407103 (accessed on 24 April 2020).
42. Epinat, B; Amram, P.; Marcelin, M. GHASP: An Hα kinematic survey of 203 spiral and irregular galaxies–VII. Revisiting the analysis of Hα data cubes for 97 galaxies. *Mon. Not. R. Astron. Soc*. **2008**, *390*, 466–504.
43. Epinat, B; Amram, P.; Marcelin, M.; Balkowski C.; Daigle O.; Hernandez O.; Chemin L.; Carignan C.; Gach J.L.; Balard P. GHASP: An Hα kinematic survey of spiral and irregular galaxies–VI. New Hα data cubes for 108 galaxies. *Mon. Not. R. Astron. Soc*. **2008**, *388*, 500–550.
44. Sofue, Y. The most completely sampled rotation curves for galaxies. *Astrophys. J.* **1996**, *458*: 120–131.
45. Sofue, Y.; Tutui, Y.; Honma, M.; Tomita A.; Takamiya T.; Koda J.; Takeda Y.. Central rotation curves of spiral galaxies. *Astrophys. J.* **1999**, *523*, 136.
46. Swaters, R.; Sancisi, R.; Van Albada, T.; Van Der Hulst, J. The rotation curves shapes of late-type dwarf galaxies. *Astron. Astrophys.* **2009**, *493*, 871–892.
47. Lehner, N.; Howk, J.C.; Wakker, BP. Evidence for a massive, extended circumgalactic medium around the andromeda Galaxy. *Astrophys. J.* **2015**, *804*, 79.
48. Sparke, L.S.; Gallagher III, J.S. *Galaxies in the Universe: An Introduction*; Cambridge University Press: Cambridge, UK, 2007.
49. Limoges, M.-M.; Lépine, S.; Bergeron, P. Toward a Spectroscopic Census of White Dwarfs within 40 pc of the Sun. *Astron. J.* **2013**, *145*, 136.
50. Limoges, M.-M.; Bergeron, P.; Lépine, S. Physical properties of the current census of northern white dwarfs within 40 pc of the sun. *Astrophys. J. Suppl. Ser*. **2015**, *219*, 19.

51. Bigiel, F.; Blitz, L. A universal neutral gas profile for nearby disk galaxies. *Astrophys. J.* **2012**, *756*, 183.
52. Izotov, Y.I.; Thuan, T.X.; Lipovetsky, V.A. The primordial helium abundance: systematic effects and a new determination. *Astrophys. J. Suppl. Ser*. **1997**, *108*, 1.
53. Vogelsberger, M.; McKinnon, R.; O'Neil, S.; Marinacci, F.; Torrey, P.; Kannan, R. Dust in and around galaxies: dust in cluster environments and its impact on gas cooling. *Mon. Not. R. Astron. Soc*. **2019**, *487*, 4870–4883.
54. Robert, J.; Gagné, J.; Artigau, É.; Lafrenière D.; Nadeau D.; Doyon R.; Malo L.; Albert L.; Simard C.; Bardalez Gagliuffi D.C.; et al. A Brown Dwarf Census from the SIMP Survey. *Astrophys. J.* **2016**, *830*, 144.
55. Holberg, J.B; Oswalt, T.D.; Sion, E.M.; McCook, G.P. The 25 parsec local white dwarf population. *Mon. Not. R. Astron. Soc*. **2016**, *462*, 2295–2318.
56. Kawka, A.; Vennes, S.; Thorstensen, J.R. Observations of white dwarfs in the solar neighborhood. *Astron. J.* **2004**, *127*, 1702.
57. Holberg, J.B; Oswalt, T.D.; Sión, E.M. A determination of the local density of white dwarf stars. *Astrophys. J.* **2002**, *571*, 512.
58. Sartore, N.; Ripamonti, E.; Treves, A.; Turolla, R. Galactic neutron stars-I. Space and velocity distributions in the disk and in the halo. *Astron. Astrophys.* **2010**, *510*, A23.
59. Elbert, O.D.; Bullock, J.S.; Kaplinghat, M. Counting black holes: The cosmic stellar remnant population and implications for LIGO. *Mon. Not. R. Astron. Soc*. **2018**, *473*, 1186–1194.
60. Maíz Apellániz, J.; Sota, A.; Arias, J.I.; Barbá R.H.; Walborn N.R.; Simón-Díaz S.; Negueruela I.; Marco A.; Leão J.R.S.; Herrero A.; et al. The galactic O-star Spectroscopic Survey (GOSSS), III: 142 additional O-type systems. Astrophysical Journal Supplement Series, **2016**, *224*, 1.
61. Arias, J.I.; Walborn, N.R.; Díaz, S.S.; Barbá R.H.; Maíz Apellániz J.; Sabín-Sanjulián C.; Gamen R.C.; Morrell N.I. Sota A.; Marco A.; et al. Spectral classification and properties of the O Vz stars in the Galactic O-Star Spectroscopic Survey (GOSSS). *Astron. J.* **2016**, *152*, 31.
62. Bartko, H.; Martins, F.; Trippe S.; Fritz T.K.; Genzel R.; Ott T.; Eisenhauer F.; Gillessen S.; Paumard T.; Alexander T.; et al. An extremely top-heavy IMF in the galactic center stellar disks. The Astrophysical Journal, **2009**, *708*, 1.
63. Maness, H.; Martins, F.; Trippe, S.; Genzel R.; Graham J.R.; Sheehy C.; Salaris M.; Gillessen S.; Alexander T.; Paumard T.; Ott T.; et al. Evidence for a long-standing top-heavy initial mass function in the central parsec of the galaxy. *Astrophys. J.* **2007**, *669*, 1024.
64. Marks, M.; Kroupa, P.; Dabringhausen, J.; Pawlowski, M.S. Evidence for top-heavy stellar initial mass functions with increasing density and decreasing metallicity. *Mon. Not. R. Astron. Soc*. **2012**, *422*, 2246–2254.
65. Kainulainen, J.; Federrath, C.; Henning, T. Unfolding the Laws of Star Formation: The Density Distribution of Molecular Clouds. *Science* **2014**, *344*, 183–185.
66. Kainulainen, J.; Beuther, H.; Henning, T.; Plume, R. Probing the evolution of molecular cloud structure-From quiescence to birth. *Astron. Astrophys.* **2009**, *508*, L35–L38.
67. Kainulainen, J.; Federrath, C.; Henning, T. Connection between dense gas mass fraction, turbulence driving, and star formation efficiency of molecular clouds. *Astron. Astrophys.* **2013**, *553*, L8.
68. Bland-Hawthorn, J.; Vlajić, M.; Freeman, K.C.; Draine, BT. NGC 300: an extremely faint, outer stellar disk observed to 10 scale lengths. *Astrophys. J.* **2005**, *629*, 239.
69. Ferguson, A.M.; Irwin, M.J.; Ibata, R.A.; Lewis, G.F.; Tanvir, N.R. Evidence for stellar substructure in the halo and outer disk of M31. *Astron. J.* **2002**, *124*, 1452.
70. McConnachie, A.W.; Chapman, S.C.; Ibata, R.A.; Ferguson A.M.N.; Irwin M.J.; Lewis G.F.; Tanvir N.R.; Martin N.; The stellar halo and outer disk of M33. *Astrophys. J. Lett*. **2006**, *647*, L25.
71. Martinez-Delgado, D.; Pohlen, M.; Gabany, R.J.; Majewski, S.R.; Penarrubia, J.; Palma, C. Discovery of a giant stellar tidal stream around the disk galaxy NGC 4013. *Astrophys. J.* **2009**, *692*, 955.
72. Ahmed, Z.; Akerib, D.; Armengaud, E.; Arrenberg S.; Augier C.; Bailey C.N.; Balakishiyeva D.; Baudis L.; Bauer D.A.; Benoit A.; et al. Combined limits on WIMPs from the CDMS and EDELWEISS experiments. *Phys. Rev. D*. **2011**, *84*, 011102.
73. Ghorbani, K.; Ghorbani, H. Scalar split WIMPs in future direct detection experiments. *Phys. Rev. D*. **2016**, *93*, 055012.
74. Bidin, C.M.; Carraro, G.; Méndez, R.; Smith, R. Kinematical and chemical vertical structure of the galactic thick disk., I.I. A lack of dark matter in the solar neighborhood. *Astrophys. J.* **2012**, *751*, 30.

75. Eker, Z.; Soydugan, F.; Soydugan, E.; Bilir S.; Gökçe E.Y.; Steer I.; Tüysüz M.; Şenyüz T.; Demircan O.; Main-sequence effective temperatures from a revised mass–luminosity relation based on accurate properties. *Astron. J.* **2015**, *149*, 131.
76. Malkov, O.Y. Mass–luminosity relation of intermediate-mass stars. *Mon. Not. R. Astron. Soc*. **2007**, *382*, 1073–1086.
77. Mann, A.W.; Feiden, G.A.; Gaidos, E.; Boyajian, T.; von Braun, K. How to constrain your M dwarf: measuring effective temperature, bolometric luminosity, mass, and radius. *Astrophys. J.* **2015**, *804*, 64.
78. Vitrichenko, E.; Nadyozhin, D.; Razinkova, T. Mass-luminosity relation for massive stars. *Astron. Lett*. **2007**, *33*, 251–258.
79. Nelson, L.A.; Rappaport, S.A.; Joss, P.C. The evolution of very low mass stars. *Astrophys. J.* **1986**, *311*, 226–240.
80. Cassisi, S.; Potekhin, A.Y.; Pietrinferni, A.; Catelan, M.; Salaris, M. Updated electron-conduction opacities: the impact on low-mass stellar models. *Astrophys. J.* **2007**, *661*, 1094.

© 2020 by the authors. Licensee MDPI, Basel, Switzerland. This article is an open access article distributed under the terms and conditions of the Creative Commons Attribution (CC BY) license (http://creativecommons.org/licenses/by/4.0/).